

A stable hothouse triggered by a tipping mechanism

Erik Chavez^{1,2,*}, Jan Rombouts³, and Michael Ghil^{4,5,6}

*Corresponding author

¹Brevan Howard Centre for Financial Analysis, Imperial College Business School, Imperial College London; London, SW7 2AZ, United Kingdom

²Laboratoire de Météorologie Dynamique (CNRS & IPSL), Ecole Polytechnique, Paris, France

³Unit of Theoretical Chronobiology, Faculty of Sciences, Université Libre de Bruxelles; Brussels, 1050, Belgium

⁴Geosciences Department and Laboratoire de Météorologie Dynamique (CNRS & IPSL), Ecole Normale Supérieure and PSL University; Paris, 75005, France

⁵Department of Atmospheric and Oceanic Sciences, University of California, Los Angeles; Los Angeles, 90095, USA

⁶Department of Mathematics, Imperial College London; London, SW7 2AZ, United Kingdom

The climate system's nonlinear dynamics is influenced by various external forcings and internal feedbacks that can give rise to regional and even global tipping points that may lead to significant and potentially irreversible changes. Paleoclimatic records reveal that Earth's climate has shifted between distinct equilibria, including a "hothouse Earth" state with temperatures about 10 K higher than at present. However, a specific mechanism for a sudden tipping to an alternate stable state, several degrees warmer than the present climate, has yet to be presented. We introduce a temperature–carbon–vegetation (TCV) model comprising an energy balance model of global temperature, coupled with global terrestrial and ocean CO₂ dynamics, and with vegetation ecosystem change. Our model exhibits a new tipping mechanism that leads to a hothouse Earth under a high-emissions scenario. Its simulations align with both observations and IPCC-class global climate models prior to tipping. The two processes that produce global tipping are: (i) temperature–albedo feedback due to darkening of the terrestrial cryosphere by glacial microalgae; and (ii) limits to vegetation adaptation that lead to reduced carbon absorption.

1 Introduction and motivation

The climate system is characterized by nonlinear and chaotic dynamics on global as well as regional scales [1, 2]. However, the relationship between the globally averaged temperature increase and cumulative anthropogenic carbon emissions is generally approximated by a linear function [3] also known as the Transient Climate Response to Cumulative Emissions (TCRE). This linear approximation is widely accepted for the present-day and moderate future emission scenarios, as reported in the 6th and most recent Assessment Report (AR6) of the Intergovernmental Panel on Climate Change (IPCC) [4]. Nonetheless, several studies also cited in the same AR6 report[4] (section 7.4.3.1 State-dependence of Feedbacks in Models) stress the limits of this proportionality relationship which no longer holds at higher atmospheric carbon levels and global temperature [5, 6]. As feedbacks could become more pronounced and climate sensitivity be state-dependent, high emission scenarios may translate into stronger warming than the TCRE predicts. Furthermore, AR6

cites studies [7, 8] that indicate "the possibility of more substantial changes in climate feedbacks, sometimes accompanied by hysteresis and/or irreversibility" that "could occur on a global scale and across relatively narrow temperature changes".

The impact of anthropogenic forcing on several of the climate system's processes has led to concern about the triggering of internal feedbacks that may lead to tipping of subsystems and its potentially irreversible consequences [1, 2, 9, 10]. The consequences of a regime shift to an extreme, Venus-like runaway greenhouse would be most dire [11] but are not very plausible. More plausible and long-lasting "hotouse" episodes have been observed in the Earth's past [12–15] and could be expected in its future [7]. One of the major sources of uncertainty is the climate system's complexity and nonlinear response to several external forcings, both natural and anthropogenic, operating at overlapping timescales[16], which could lead to such type of global-scale changes. However, specific mechanisms for rapid global tipping to a hothouse Earth have not been explored so far to a satisfactory extent [17–19] and remain quite uncertain, as stressed by the AR6 [4]. Representing fundamental uncertainties in future temperature values and other key climate features [20] is essential for shaping mitigation and adaptation policy [21, 22].

Accurately simulating and predicting major nonlinear features of the climate system remains quite challenging, in spite of significant progress [23, 24]. Complementary modeling approaches to ESMs have proven useful in contributing to understand these nonlinear dynamics. The approach of "emergent constraints," for instance, integrates observational data and reconstructed paleoclimate proxies [25–27]. An alternative method employs a hierarchy of models to address specific aspects of the climate system [28, 29].

Thus, Held (2005) [30] argues that the leaps molecular biology has achieved in understanding complex systems like the human organism are largely due to the systematic and constant study, validation, and integration of hypotheses and learning from the lower rungs of the biological model hierarchy into the higher rungs. Their use is also valuable in the climate sciences to better understand and predict the response of more detailed ESM models [2, 10, 31].

In the climate science, the initial rung of the model hierarchy is that of global energy balance models (EBMs) [32–36] that can track the evolution of the globally averaged temperature subject to changes in radiative in- and output. Similar simple models with a few scalar variables have been used to characterise nonlinear phenomena such as bistability [37] and chaotic behavior [38] in the oceans or atmosphere, as observed in the Earth's paleoclimatic records [39].

Following the evolution of atmospheric carbon concentration on different timescales also requires the modeling of carbon fluxes through the Earth's subsystems [40, 41]. The lowest rung in the carbon model hierarchy is that of using a small number of boxes. Typically, these boxes encompass the atmosphere, the land soil and the vegetation, the upper ocean, and the deep ocean. Accordingly, two- [42], three- [43], four-[40, 44, 45] or even eight-box models [46] have been proposed. Such simplified models do not account for spatially heterogenous dynamics but can still be successful at reproducing the global dynamics of the underlying processes, including carbon uptake by vegetation. For instance the zero-dimensional (0-D) models developed by Lade et al [44], Svirzhev and von Bloh [42], or Smith et al [47], allow one to capture essential feedback mechanisms between global vegetation and climate.

No coupled EBM model on human timescales, though, has — to the best of our knowledge — described abrupt tipping mechanism in the climate system from the present state to a stable hothouse, in which the Earth's climate would stabilize at roughly 10 K above the current climate, as conceptually proposed by Steffen et al. [7], and in line with paleoclimatic proxies [12]. Ghil [35] showed, in fact, that a spatially one-dimensional EBM with temperature dependent solely on latitude and time can yield a pole-to-equator steady-state profile in very good agreement with seasonally averaged mid-20th century temperatures. Furthermore, EBMs such as these have helped

study the double-fold bifurcation giving rise to an alternative steady state called, at the time, a “deep freeze.” [34–36] The theoretical prediction of such a state was subsequently confirmed through geochemical analysis of Neoproterozoic and other paleoclimatic records [48], and is called now a “snowball Earth”. Encouraged by this and other successes of such models [10, 43, 44], we formulate herein a 0-D model coupling the evolution of global average temperatures with global carbon levels and a global vegetation index.

The purpose of this paper is to study a fundamental source of uncertainty in the future trajectory of the climate system in response to anthropogenic carbon forcing; namely the likelihood of a potential planetary regime shift or tipping that could take the system into an alternate but plausible regime of behavior [10, 49]. In this study, we identify a tipping mechanism that relies on two specific and credible biogeophysical feedback processes.

Clearly, confidence in our results needs to be tempered by the simplicity of the model and seen in the perspective of the aforementioned hierarchy of models. Global EBMs and idealized coupled models like ours are able to exhibit planetary-scale tipping when their few state variables permit including feedback processes that may lead to saddle-node [35] or Hopf [50] bifurcations. Spatial averaging in EBMs and box models, however, mutes heterogeneity, which leads to loss of the ability to capture tipping when one or more regions exceed local thresholds, jointly or independently.

High-resolution ESMs, though, can resolve such heterogenous processes leading to the potential crossing of regional thresholds, such as in ecosystem shifts [1]. Their use thus allows one to study potential tipping of regional subsystems [1] but their high resolution in today’s IPCC-class models, of the order of 10^9 scalar variables for a mesh size of $0.25 \text{ deg} \times 0.25 \text{ deg} \times 0.2 \text{ km}$, makes their results much less transparent, as do the tens of parameters [51] used in fitting their various unresolved processes to the climate of the 150 years of the instrumental era.

Moreover, the numerical diffusion of ESMs, as well as their limited run length due to computational cost, can also postpone or damp a genuine global bifurcation [52]. Therefore, low-dimensional models such as those used herein can reveal and help characterize dynamic bifurcations, while ESMs with high spatial resolution allow one to explore regional tippings that may, or may not, aggregate into a global regime change. The two ends of the model hierarchy can thus complement each other. Reduced models help explore potential tipping mechanisms of the global climate system, while high-resolution models supply the spatially explicit representation of these mechanisms that is needed to calibrate and refine the reduced-model results [28–30].

2 A model for coupled globally averaged temperature and carbon dynamics

Our 0-D EBM is based on the 0-D version [53] of the original, spatially one-dimensional EBM of refs. [33, 35], coupled to a three-box carbon model. This coupled model is based on physical, chemical and biological processes that operate on the decadal timescales of interest in the adaptation and mitigation problem [22]. More precisely, the model’s energy balance separates ocean from land albedo, following Källen et al. [50].

Encouraged by the performance and high tractability of the framework presented by Lade et al.[44], we adopt its choice of global-level carbon fluxes representation. Our modelling of the terrestrial carbon sink’s global dynamics relies on the Carnegie-Ames-Stanford biosphere model [54], on the 0-D formulation of vegetation carbon uptake in ref. [42], and on the global terrestrial respiration’s temperature sensitivity as in ref. [55]. In order to represent the 0-D global carbon dynamics of the ocean sink, we rely on detailed studies of the carbon cycle in the ocean [44, 56, 57].

The coupled model is designated as the TCV model, for its key global variables: temperature, carbon content, and vegetation. Its parameter values are based on output of IPCC-class model simulations and on observational data; see the three Tables with model parameters in the Supplementary Material.

This biogeophysical TCV model is governed by a set of four ordinary differential equations (ODEs): Eq. (1a) for the evolution of the globally averaged atmospheric and near-surface ocean temperature T ; Eq. (1b) for the evolution of atmospheric carbon stock C_A ; Eq. (1c) for the evolution of the carbon stock C_M in the ocean's mixed layer; and Eq. (1d) for the level V of degradation of the land vegetation. The full four-ODE model is given by:

$$c\dot{T} = Q_0 (1 - p\alpha_L(T) - (1 - p)\alpha_O(T)) - \kappa(T - T_\kappa) + a \ln(C_A/C_0), \quad (1a)$$

$$\dot{C}_A = -F_{A \rightarrow L}(T, C_A, V) - F_{A \rightarrow M}(T, C_A, C_M) + e(t), \quad (1b)$$

$$\dot{C}_M = F_{A \rightarrow M}(T, C_A, C_M) - F_{M \rightarrow D}^P(T, C_M) - F_{M \rightarrow D}^B(T, C_M), \quad (1c)$$

$$\dot{V} = -\mu V(1 - V) + f(T)(1 - V). \quad (1d)$$

The temperature equation (1a) is governed by the balance between incoming radiation R_i and outgoing radiation R_o . The incoming radiation from the sun Q_0 is modified by the albedo α_L of the land and α_O of the ocean, which in turn depend on the temperature T ; the fraction of land is given by p . The outgoing radiation $R_{out} = \kappa(T - T_\kappa)$ is diminished by the greenhouse effect due to the atmospheric CO₂ concentration C ; this effect is given by $a \ln(C_A/C_0)$, with C_0 the preindustrial value of C_A , and a the intensity parameter of radiative forcing [58]. Note that C_A and C differ by a constant factor, since the volume of the atmosphere can be assumed to be fixed on these timescales. The heat capacity c in this equation is taken equal to that of the atmosphere and ocean mixed layer combined, since we are interested here in global temperature variations on the time scales of years to decades.

In equation (1b), $F_{A \rightarrow L}$ captures the flux of atmospheric carbon into the terrestrial carbon sink, while $F_{A \rightarrow M}$ captures the carbon flux from the atmosphere to the ocean mixed layer. In this equation, $e = e(t)$ is the anthropogenic GHG forcing, expressed in GtC/yr of carbon equivalent, with $e(0) = 0$ and $t = 0$ in the year 1800.

In equation (1c), $F_{M \rightarrow D}^P$ captures the flux of carbon from the ocean mixed layer to the deeper ocean through the physical effect of the temperature-dependent overturning circulation, while $F_{M \rightarrow D}^B$ captures the flux of carbon to the deeper ocean due to the biopump associated with Wallace Broecker's name [59]. All these carbon fluxes depend in the model on the global temperature T .

Equation (1d) describes the evolution of V , a proxy for ecosystem degradation. Its evolution depends on temperature and the equation is derived from a modified logistic growth equation. The function $f(T)$ models how high temperatures lead to vegetation loss, and μ dictates the timescale of recovery; see the Methods section for further details.

In order to understand our TCV model's behavior in a more transparent, graphical way, we first reduce the four-ODE system (1) to a three-ODE system (2), by assuming a fast equilibration [60] across the ocean surface of the carbon concentrations, and hence of C_A and C_M ; the two ODEs (1b) and (1c) above are thus reduced to a single ODE (2b) and to the algebraic equation (2d) below. For the details of the model reduction, see the Methods section. In the next section, we will first analyze the model's behavior for fixed V . In this case, we have a system of two ODEs and one algebraic equation, whose steady states can be studied graphically in the system's phase plane.

The reduced differential-algebraic system of equations (DAE) below couples the evolution of T

and of the total atmospheric and mixed layer carbon $C_S = C_A + C_M$:

$$c\dot{T} = Q_0 (1 - p\alpha_L(T) - (1 - p)\alpha_O(T)) - \kappa(T - T_\kappa) + a \ln(C_A/C_0), \quad (2a)$$

$$\dot{C}_S = -F_{A \rightarrow L}(T, C_A, V) - F_{M \rightarrow D}^P(T, C_M) - F_{M \rightarrow D}^B(T, C_M) + e(t), \quad (2b)$$

$$\dot{V} = -\mu V(1 - V) + f(T)(1 - V). \quad (2c)$$

$$0 = F_{A \rightarrow M}(T, C_A, C_M). \quad (2d)$$

We refer to this simplified DAE version of the TCV model as TCV-DAE for short. The parameter values used in the equations above are listed in Tables S1, S2, and S3, and the annual anthropogenic emissions $e(t)$ are expressed in GtC/yr of carbon equivalent.

Both the full, four-ODE model (1) and the reduced, DAE version (2) allow one to reproduce reliably historical globally averaged temperature and carbon fluxes to the ocean and land and are in agreement with IPCC-class ESMs simulations of global averages of these temperature and carbon fields. Moreover, our model captures two essential, regional mechanisms that drive the tipping from the current, mild climate to a stable hothouse. These two biogeophysical mechanisms are part of the Earth system's response to increased atmospheric GHG concentrations, namely:

- (i) the self-sustained rapid darkening of the terrestrial cryosphere due to glacial microalgal growth [61–63] that drives the decrease of planetary albedo; and
- (ii) the limited ability of land vegetation to adapt to the higher temperatures that will prevail,[64–66], and that will decrease therewith its carbon absorbing capacity.

The way that these mechanisms enter equations (1a) or (2a) for mechanism (i) and (1d) or (2c) for mechanism (ii), respectively, is described in the Methods section.

3 Results

The predictive robustness of the proposed TCV model is first tested by comparing its simulations with historical data, as well as with the simulations of IPCC-class GCMs subject to several anthropogenic emissions scenarios (Fig. 1). The good approximation by TCV model simulations of observations and IPCC-class model simulations allows one to validate its soundness and usefulness in studying how the addition of a feedback process not currently included in IPCC-class models might affect global temperature–carbon dynamics (Fig. 2). Here, we integrate in the TCV model the effect of terrestrial darkening due to mechanism (i) above that is currently not included in ESMs [31].

Subsequently, we show that the TCV model, has two distinct stable steady states, and illustrate how this leads to tipping when it is forced with increased anthropogenic carbon emissions such as in Representative Carbon Pathway (RCP) 8.5 scenario. The coupled DAE model of system (2) above is simple enough to analyze graphically, yet includes the just described physical and biogeochemical processes that operate at the decadal timescales of interest in adaptation to and mitigation of climate change [22, 31]. In the absence of time-dependent forcing, the model exhibits a single stable fixed point P_1 that corresponds to the present climate. The presence of anthropogenic forcing can then give rise to an additional fixed point P_2 , which corresponds to a stable hothouse that lies about 10 K above the present global temperature; the two points P_1 and P_2 lie at the left- and rightmost intersection of the two nullclines in Fig. 3.

The transitions between these two stable steady states, the current climate and the hothouse, will be studied next, in connection with Fig. 4. In spite of its simplicity, when forced with several

RCPs, our 0-D TCV model produces results that are close to three-dimensional GCMs and ESMs, as shown in section “Time evolution of the model under anthropogenic forcing” below. Moreover, by including the representation of ecosystem loss in equations (1d) or (2c), the phenomenon of climate commitment [67, 68] — the temperature warming locked in without any further anthropogenic forcing — is likewise captured, as seen in Fig. 5 .

TCV model evaluation vs. observations and high-end model simulations

The parsimonious formulation of our TCV model relies on functional forms for the processes included that are derived from validated representations of each relevant field, as shown in the Methods section. The model’s realism is supported by the choice of model parameters values. All of them are extracted from refereed publications based on detailed observational studies or on high-end model simulations. The corresponding references are listed in Table S1 for the energy balance equation (1a), in Table S2 for the flux of carbon into the terrestrial carbon sink in Eq. (1b) and environmental degradation in Eq. (1d), and in Table S3 for the flux of carbon into the ocean carbon sink of (1c). All the parameter values in this paper lie within the corresponding confidence intervals reported in the references cited in these tables.

The accuracy and robustness of the model so obtained is evaluated by comparing its simulations with both observational data and IPCC-class GCM simulations subject to several RCP carbon emission scenarios. Figure 1 displays the comparison of the TCV model (in red) with globally and annually averaged observed temperatures (blue) from year 1880 to year 2022 in panel (a); in panels (b)–(d) with the ensemble mean (black) of up to 42 different GCMs subject to RCP 2.6, 4.5, and 6.0, from 1861 to 2100; and in panel (e) for RCP 8.5 up to the point of the global tipping shown in Fig. 6(c) of the next subsection.

The difference between the TCV model and the observed temperatures or the ensemble mean of the 42 GCMs is measured by the root-mean-square error (RMSE). This measure is used to compare the performance of each GCM against observations as well. The TCV model has the 7th lowest RMSE amongst the 42 GCMs when compared with the observed instrumental temperatures. It ranks either as highly as an average GCM or better when compared with the ensemble mean for each of the four RCP scenarios. The Bland-Altman plots [69] show that median difference between the TCV model’s simulated temperatures and the global mean observational data is lower than 0.1 K; see Fig. S2. Moreover, the Bland-Altman scatter plots in the figure show that the TCV model’s global temperature estimates are in agreement with those of the set of the 42 IPCC-class GCMs.

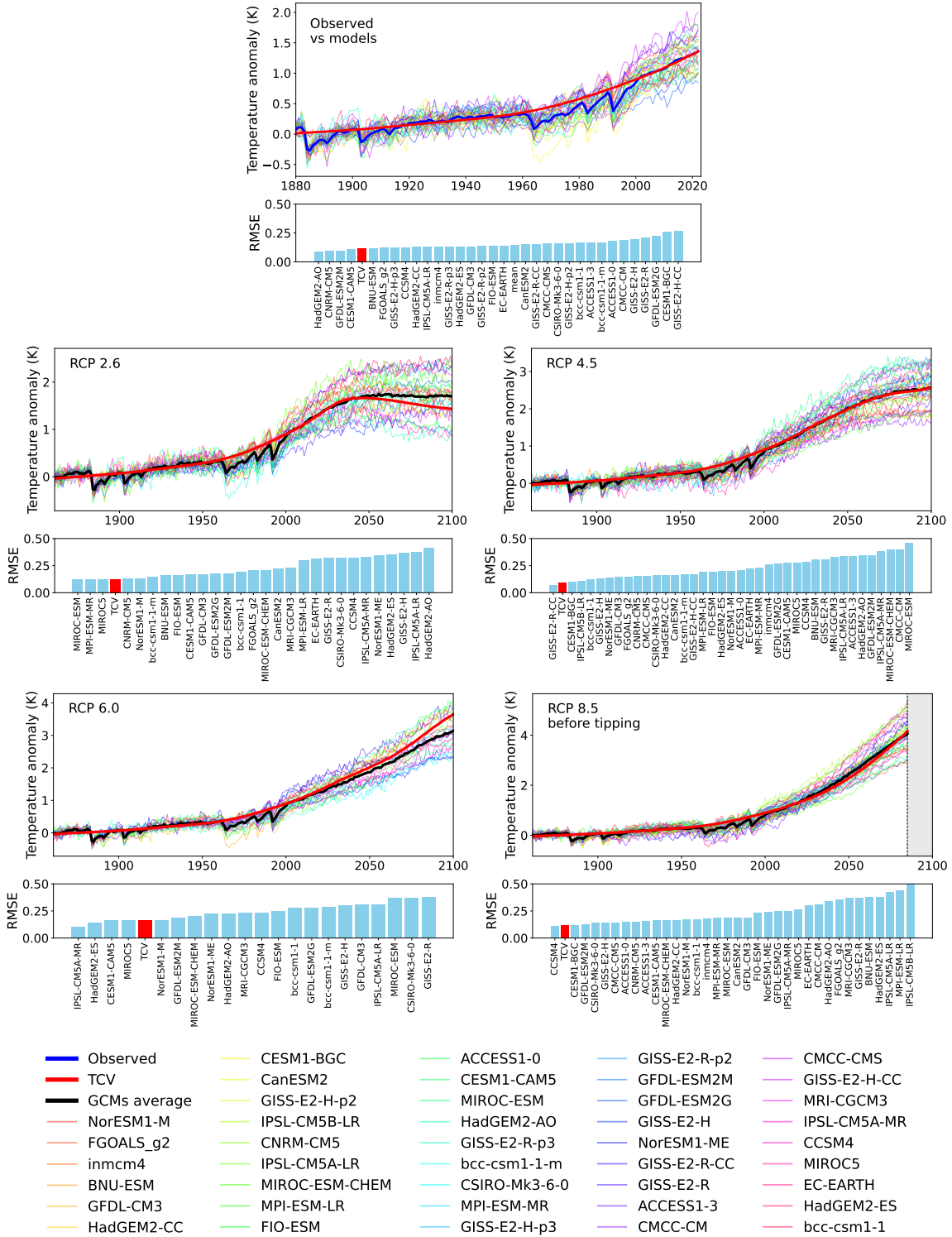


Figure 1: TCV model validation with respect to observational data and IPCC-class GCM simulations. In each panel, the TCV model's temperature simulation (heavy red line) is compared with observational data (heavy blue line), as well as with 42 different IPCC-class GCM models (light colors) subject to four RCP scenarios [70] and with their ensemble mean (heavy black line). The TCV model is benchmarked against individual GCMs using its RMSE with respect to either (a) observed data or (b–e) the GCM ensemble mean.

The carbon fluxes of the TCV model are assessed by comparing them with global estimates from 1959 to 2021 obtained by high-end carbon models included in the Global Carbon Project (GCP) [71]: 11 models for the terrestrial fluxes and 16 for the ocean fluxes; see Fig. S3. Panels (a) and (b) clearly show the large scatter of GCP model simulations, for both ocean and land fluxes, respectively. In panels (c) and (d), we consider more systematically this scatter and the TCV model performance. The mean of the differences at each point in time between the largest and the smallest fluxes in the GCP models equals 0.85 GtC/yr for the ocean fluxes and 2.83 GtC/yr for the terrestrial fluxes (dashed red line in the panels) vs. the RMSE between the TCV model and GCP models, which is below 0.5 GtC/yr for half the ocean fluxes — namely for the CNRM, MPI, IPSL, Princeton, and CESM-ETHZ models, see Fig. S3(e) — and equal or less than 1.6 GtC/yr for 6 of 16 of the land flux models — namely OCNv2, CLM5.9, JSBACH, ISAM, CABLE-POP, and VISIT models; see Fig. S3(f).

Therefore, the TCV model’s simulations and the results of their validation confirm the robustness of its underlying representation of the different biogeochemical processes included in the model. Further statistical validation tests are provided in the Supplementary Material on “TCV model evaluation: further tests.”

Based on these results, we proceed to assess the effect on global temperature-carbon dynamics of the inclusion of potential terrestrial albedo darkening by glacial algal blooms [61, 72, 73] on the land cryosphere, a mechanism that is not currently included in IPCC-class GCMs. To do so, the terrestrial albedo darkening is evaluated based on the use of output from simulations of the CNRM-CM5 climate model coupled with the ISBA-ES snowpack dynamics and hydrology model [74, 75]. Figure 2 displays the grid-level surface albedo prior to algal darkening (Fig. 2(a)) and following maximum darkening (Fig. 2(b)). The globally averaged value is computed while accounting for latitudinal gradients (see Fig. S7) of annual cumulative radiation and the latitude dependence of gridded areas in order to parametrize the α_{\max}^L (Fig. 2(a)) and α_{\min}^L (Fig. 2(b)) values of the temperature-dependent terrestrial albedo $\alpha_L(T)$ function (see Eq. (S3)) of Eq. (1a). Further details are provided in the Methods section.

The TCV-DAE model’s two stable steady states

In the absence of anthropogenic GHG emissions, i.e., with $e = 0$, and for the chosen parameter values in Tables S1–S3, the TCV model has only one stable steady state corresponding to our current climate’s equilibrium plotted as a blue-filled circle in Fig. 3(a). When the level of atmospheric carbon e is increased by anthropogenic annual emissions to a value above 16 GtC/yr, while still using $V = 0$, two stable steady states, separated by an unstable one, co-exist. The two stable steady states are plotted as filled blue and red circles, respectively, in Figs. 3(b) and 3(c).

The present climate is denoted henceforth in the text by $P_1 = (T_1, C_1) = (286.5 \text{ K}, 1,505 \text{ GtC}) = (13.4 \text{ }^\circ\text{C}, 284 \text{ ppm})$; see Fig. 3(a). The stable hothouse steady state shown in 3(c) for $e = 21 \text{ GtC/yr}$ and $V = 0$ appears for higher levels of carbon emissions and is denoted by $P_2 = (T_2, C_2) = (295.8 \text{ K}, 2,071 \text{ GtC}) = (22.7 \text{ }^\circ\text{C}, 617 \text{ ppm})$. The eigenvalues associated with the linearization of the TCV-DAE model at these two fixed points are all real and negative: for P_1 they are given by $(\lambda_{1,P1} = -0.11, \lambda_{2,P1} = -0.07)$, while for P_2 they are $(\lambda_{1,P2} = -0.14, \lambda_{2,P2} = -0.05)$.

Note that the nullclines in Fig. 3 have discontinuities in the derivatives, because of the piecewise linear character of several terms in the right-hand sides of the ODEs; see Methods section. This property does not invalidate in any way the conclusions we draw from the figure. In particular, all the fixed points lie at the intersections of nullcline segments that are continuously differentiable. Hence the positions of these points in the model’s phase-parameter space depend also smoothly on the model’s parameters, at all but the bifurcation points themselves, where the one-sided derivatives

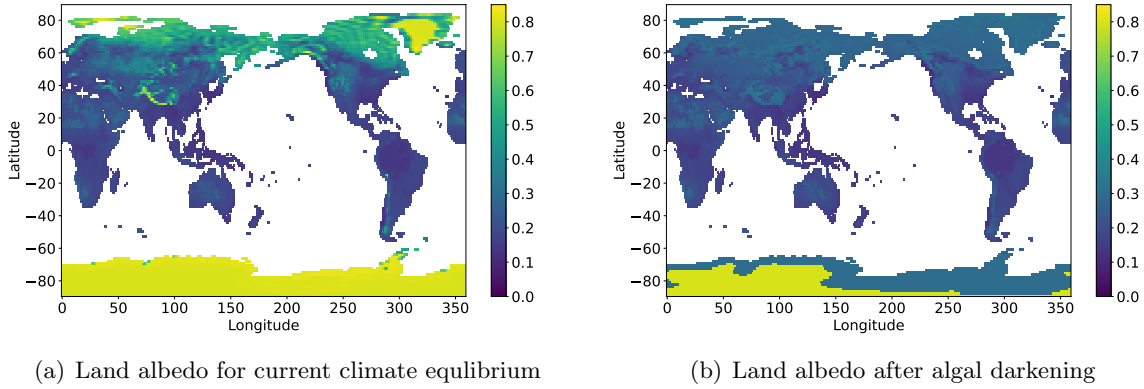


Figure 2: Global terrestrial surface albedo darkening. Plots of climatological terrestrial albedo with and without algal darkening of ice sheets and midlatitude cryosphere. Grid-level values were computed using raw data from simulations of the CNRM-CM5 climate model coupled with the ISBA-ES snowpack dynamics and hydrology model [74, 75] for the 2070–2100 interval, subject to the RCP 8.5 emission scenario. Panel (a) displays grid-level annual climatological terrestrial albedo with no algal darkening; and panel (b) displays grid-level albedo with maximum darkening of land cryosphere due to algal blooms. The minimum and maximum global average terrestrial albedo values used in $\alpha_L(T)$ of Eq. 1a (see Eq. S3 in Methods) are obtained after performing a weighted spatial average of gridded data in (a) and (b) accounting for both the latitudinal gradient of annual cumulative radiation and the latitude dependence of gridded areas; see Fig. S7 and Methods section.

exist but are unequal between one side and the other.

The unstable fixed point $P_3 = (T_3, C_3)$ that separates P_1 from P_2 is marked by an orange-filled circle in both panels. The corresponding eigenvalues are one positive and one negative: at $e = 21$ GtC/yr they are $(\lambda_{1,P3} = +0.20, \lambda_{2,P3} = -0.10)$.

The yearly carbon equivalent flux of $e = 21$ GCt/yr that is only reached in RCP8.5 was chosen for panels (b) and (c) of Fig. 3 for illustrative purposes, to showcase the coexistence of three steady states. As shown hereafter in Fig. 4(a), even for $V = 0$ three steady states coexist already from $e = 16$ GtC/yr on.

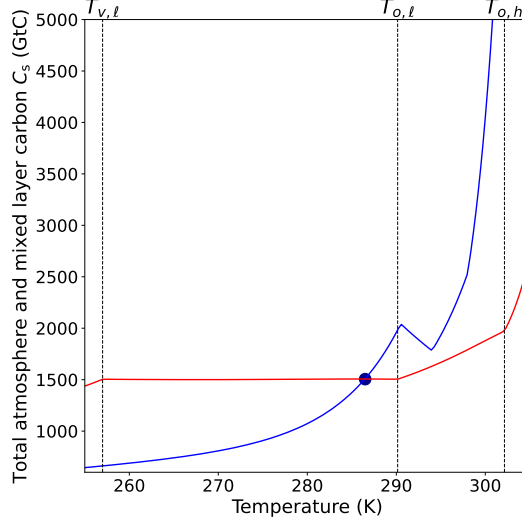
A more complete understanding of the model behavior's parameter dependence is obtained by considering the bifurcation diagrams in Fig. 4. These show the temperature of the model's steady states and their stability as a function of e , considered here as a parameter with prescribed values; $e = 0$ in the diagrams corresponds to the preindustrial climate state, with $T = 286.5$ K [76].

In Fig. 4, we concentrate on the dependence of the current climate P_1 and the hothouse P_2 on the annual GHG emissions e , and plot $T_j = T_j(e)$ for $j = 1, 2, 3$, shown as solid light blue and light red lines for the two stable steady states, $j = 1, 2$, respectively. The unstable intermediate branch that corresponds to $j = 3$ is dashed and black.

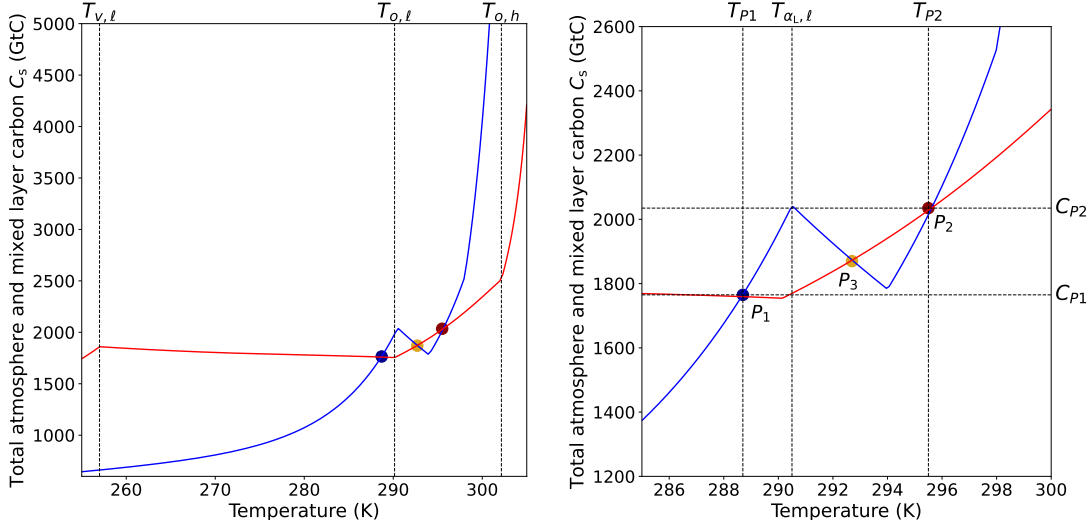
The bifurcation diagrams herein correspond roughly to the double-fold bifurcation. The curved arrows — shown in Fig. 4 in dark blue for the upward portion of the hysteresis cycle and in dark red for its downward portion — correspond to the heavy solid segments of the hysteresis cycle. The bifurcation points in Fig. 4 are denoted by B_c and B_d , and shown as blue- and red-filled circles, respectively.

As e increases, the steady state corresponding to current climatic conditions disappears at B_c , at an emission level $e_c = 31.5$ GtC/yr for $V = 0$, and the system jumps onto the hothouse branch of solutions. Note that, for the more deteriorated land vegetation in Fig. 4(b), this bifurcation is reached at a much lower value of the annual emissions, namely $e_c = 21.5 < 31.5$ GtC/yr. A

full return to current conditions once the hothouse state is reached requires a decrease of annual emissions, possibly complemented by new or enhanced carbon sinks, to remove carbon below $e_d = 16.5$ GtC/yr, all the way to the red dots in Figs. 4(a) and 4(b). This discrepancy between e -values



(a) Phase portrait for $e = 0$ GtC/yr and $V = 0$



(b) Phase portrait for $e = 21$ GtC/yr and $V = 0$. (c) Blow-up of (b) for $e = 21$ GtC/yr and $V = 0$.

Figure 3: Phase portrait of the coupled DAE model (2) for two emissions levels, $e = 0$ and $e = 21$, and constant ecosystem degradation level, $V = 0$. The coordinates are global temperature T in degrees K on the abscissa and total surface carbon C_S in GtC on the ordinate. The temperature and carbon nullclines $F_1(T, C_S) = 0$ and $F_2(T, C_S) = 0$ that correspond to equations (2a) and (2b) are in blue and red, respectively. (a) The phase portrait for preindustrial conditions; (b) the phase portrait for $e = 21$ GtC/yr that illustrates the model's three steady states; and (c) blow-up of area in panel (b) that contains the model's three steady states. The blue-filled circle indicates the stable current climate P_1 (left) and the red-filled circle corresponds to the hothouse climate P_2 (right), with the unstable fixed point P_3 in orange in-between. The light vertical line in all three panels indicates a discontinuity in the derivative of α_O at $T_{\alpha,\ell} = 290$ K that is explained in the Methods section; in panel (c) the temperatures T and carbon stock C_S of the two stable steady states are also indicated by light dashed lines.

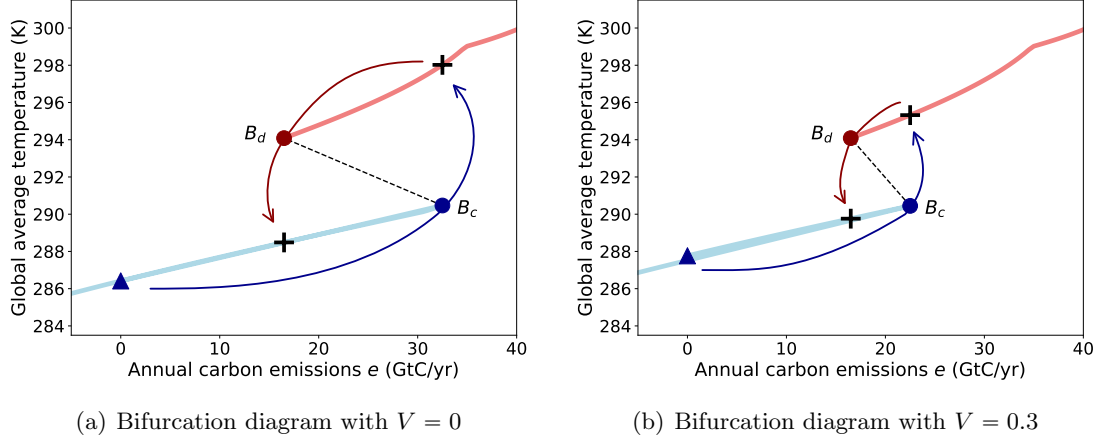


Figure 4: **Bifurcation diagrams of the TCV-DAE model with fixed vegetation degradation V .** The two diagrams show the steady states' temperature T as a function of the yearly carbon emissions e : (a) for intact ecosystems, $V = 0$; and (b) for nonzero ecosystem degradation, $V = 0.3$. In both panels, the stable branches are light blue for the current climate and light red for the hothouse; the intermediate, unstable solution branch is dashed black. The dark blue triangle indicates the preindustrial steady state P_1 for the standard parameter values of Tables S1, S2, and S3. The bifurcation point of the current climate P_1 and intermediate branch P_3 is shown as a filled blue circle B_c with coordinates $(T_c = 290 \text{ K}, e_c = 31.5 \text{ GtC/yr})$ for $V = 0$ and $(T_c = 290 \text{ K}, e_c = 21.5 \text{ GtC/yr})$ for $V = 0.3$, while the other bifurcation point B_d , shown as a filled red circle, has coordinates $(T_d = 294.2 \text{ K}, e_d = 16.5 \text{ GtC/yr})$ for both $V = 0$ and $V = 0.3$.

for the upward and the downward jump between climate branches is part of the hysteresis cycle associated with the tipping.

Note that in usual saddle-node bifurcations [77–79], where the transition between the stable and the unstable branch is smooth, one of the two eigenvalues of the governing ODE system's linearization goes through zero and changes sign. Here, instead, the eigenvalue that distinguishes between the stable nodes all along the branch of the current climate and the saddles all along the unstable branch jumps from a negative to a positive value at the bifurcation point, without crossing zero; see `TCV_video-V=V(t)` video in the Supplementary Material.

The geometry of the nullclines in Figs. 3 and `TCV_video-V=V(t)` reveals that the merger of the stable and unstable fixed points P_1 and P_3 occurs when the global temperature T reaches $T_{\alpha_{L,\ell}}$, at which point the darkening of the cryosphere due to algal blooming starts to increase, causing the percentage of incoming radiation Q_0 absorbed by Earth's surface to increase, too. This increase leads to the upward jump of the climate from the current climate branch to the hothouse branch. The leftmost red-filled dot in Fig. 4, which occurs at $e_d = 16.5 \text{ GtC/yr}$ for both $V = 0$ and $V = 0.3$, corresponds to the merger of the stable and unstable fixed points P_2 and P_3 that occurs when the global temperature T reaches $T_{\alpha_{L,u}}$, triggering a jump from the stable hothouse branch of solutions back to the current climate branch.

We assessed the robustness of the two-steady-state regime by using two complementary sensitivity analyses. First, in an one-at-a-time (OAT) sweep, we varied every temperature parameter by $\pm 4 \text{ K}$ and every non-temperature parameter by $\pm 20\%$ around the values in Tables S1, S2, and S3; bistability persisted for 37 of 39 parameters, with its sensitivity confined to the terrestrial albedo bounds α_{\min}^L and α_{\max}^L .

Second, we applied a variance-based Sobol analysis [80–82] to the albedo-calibration subset given by Eqs. (2) and (S3). This analysis addressed the probability of bistability at $V = 0$ and

showed that α_{\min}^L is the dominant contributor, capturing a “first-order sensitivity, or main-effect, index” $S_1 \simeq 0.39$ of the variance on its own, with $\sim 28\text{--}49\%$, and a “total-effect index” of $T \simeq 0.79$, including interactions, with $\sim 70\text{--}89\%$. The second factor, α_{\max}^L , exhibits a main effect $S_1 \simeq 0.16$, with $\sim 9\text{--}21\%$, and a total effect $T \simeq 0.53$, with $\sim 42\text{--}63\%$. Fig. S6 indicates that the interactions-driven sensitivity is driven primarily by pairwise $\alpha_{\min}^L \times \alpha_{\max}^L$ parameters joint variation; the contrast between terrestrial albedo bounds, contributing $\sim 25\%$ of the total $\sim 70\text{--}89\%$.

The threshold temperatures contribute but little to the sensitivity: for $T_{\alpha_L, \ell}$, $S_1 \simeq 0.02$, with $\sim 0\text{--}5\%$, and $T \simeq 0.20$, with $\sim 15\text{--}25\%$, while for $T_{\alpha_L, u}$, $S_1 \simeq 0$, with $\simeq 0\text{--}2\%$, and $T \simeq 0.13$, with $\sim 8\text{--}18\%$; see Fig. S5. Thus, the model’s albedo bounds, α_{\min}^L and α_{\max}^L , themselves exhibit pronounced differences in their main and total effects, S_1 and T , while the temperature thresholds have overall a small impact on the bistability. Together with the OAT results in Fig. S4, this identifies the terrestrial minimum albedo as the primary control on bistability, with a secondary direct role for the maximum albedo.

Time evolution of the model under anthropogenic forcing

So far we considered the behavior of our TCV model for a fixed $e = 0$ and $e = 21 \text{ GtC/yr}$, as illustrated in Fig. 3, and for distinct values of e , each of which is fixed in time, as shown in Fig. 4. We next subject our coupled TCV-DAE model, using a terrestrial vegetation degradation $V(t)$ that evolves according to equation (2c), to anthropogenic forcing that corresponds to a prescribed function $e = e(t)$. We rely here on the RCP scenarios of GHG emissions, measured in carbon-equivalent concentrations, which were used in the most recent IPCC assessment reports [83].

The resulting temperature evolution for each of the RCPs are displayed in Fig. 5(a) for the parameter set of Tables S1 –S3. In the more moderate RCPs 2.6, 4.5, and 6.0, the increase in emissions leads to increases in the average global temperature as well of atmospheric carbon concentration [84] and carbon fluxes across the land and ocean sinks that are comparable to observational datasets [71], as well as to those obtained in high-end model simulations of successive IPCC assessment reports.

Similarly, the model fluxes of carbon to the separate sinks of the coupled atmosphere-land-ocean system are comparable with observations and with simulations obtained from high-end models, as displayed in aggregated form in the comprehensive Global Carbon Budget [71]. The fluxes of carbon from the atmosphere to the oceanic mixed layer and to the land vegetation, as well as the evolution of atmospheric carbon stock are displayed in Figs. 5(b,c,d), respectively.

In Fig. 5(a), the noticeable plateauing of global temperature at a higher level following anthropogenic GHG forcing is consistent with the recalcitrant warming simulated by more detailed climate models [67, 68]. In the present model, it is the degradation of the land vegetation’s carbon sink capacity that underlies this climate commitment; see Methods section.

We carried out numerical simulations of model trajectories starting near the present climate P_1 for anthropogenic emission scenarios given by RCPs 2.6, 4.5, 6.0 and 8.5 [83, 86], using both the full and the reduced versions of our TCV model. The model reproduces accurately the trajectory of global average temperatures T , as well as global land vegetation and ocean carbon fluxes $F_{\text{A} \rightarrow \text{L}}$ and $F_{\text{A} \rightarrow \text{O}}$, based on both observations and high-end, IPCC-class climate and carbon cycle models for the low, moderate, and moderately high RCPs 2.6, 4.5 and 6.0; see Fig. 5. In fact, the differences between the simulations using our model’s full and reduced versions are truly minimal.

For the most severe anthropogenic GHG emission scenario, namely RCP 8.5, a gradual increase in temperatures from preindustrial values leads in a few decades’ time from now to an upward jump of roughly 8 K as the Earth transitions to the hothouse steady state, as shown in Fig. 6(c). As discussed in connection with Fig. 4 above, this jump appears to be irreversible unless one

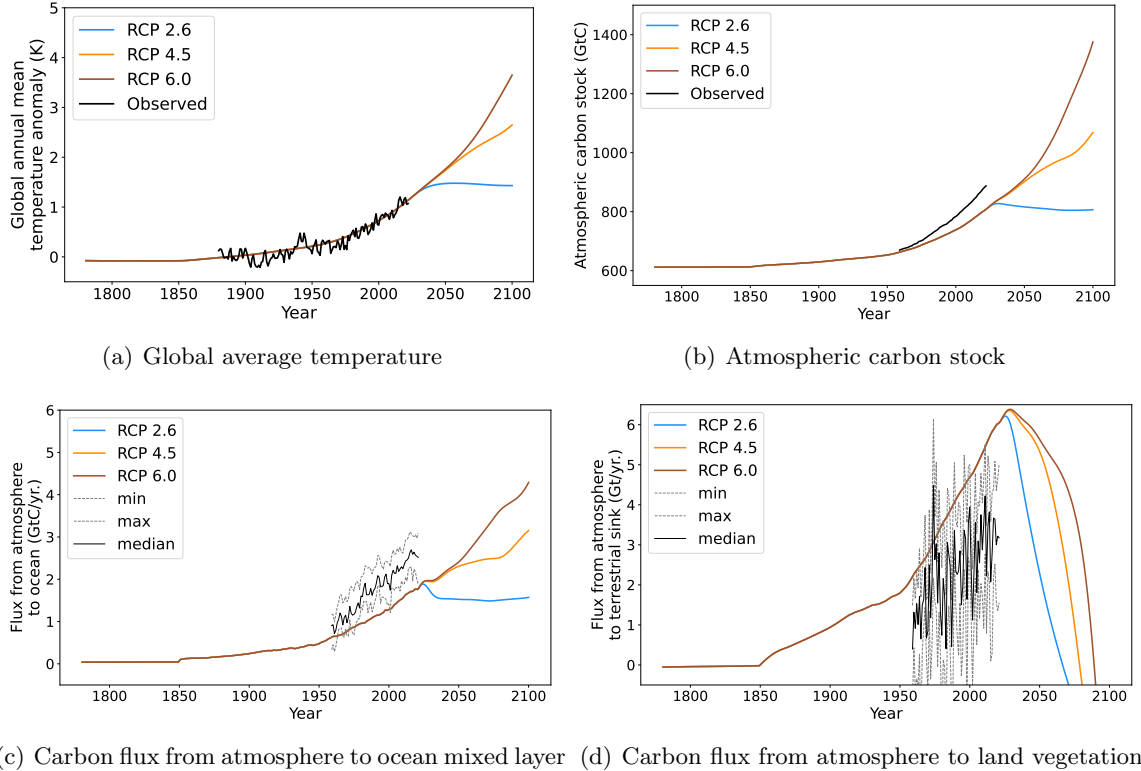


Figure 5: Evolution of the global temperature anomalies, carbon stocks, and carbon fluxes in our TCV model with anthropogenic forcing. The parameter values used are given in Tables S1, S2, and S3. and the results are shown for Representative Carbon Pathways (RCPs) RCP 2.6 (blue), RCP 4.5 (orange), and RCP 6.0 (brown) [83]. Preindustrial initial state is ($T_0 = 286.5$ K, $C_{A,0} = 589$ GtC). (a) Temperature anomaly evolution, with observed anomalies in solid black [85]; (b) atmospheric carbon stock C_A , with observed stock in solid black [71]; (c) Fluxes $F_{A \rightarrow O}$ to the ocean mixed layer; and (d) fluxes $F_{A \rightarrow L}$ to the land vegetation. The minimum (dashed), maximum (dotted) and median (light solid) lines in panels (c) and (d) are based on different observation and model-based estimates of carbon fluxes aggregated in the Global Carbon Budget [71].

considers much augmented carbon sinks, along with carbon capture and storage technologies [22]. The present TCV model suggests that fairly substantial decreases of e below preindustrial values, denoted here by $e = 0$, would be required to do so.

The effects of gradual changes in GHG emissions on the increase in temperatures are illustrated in Figs. 5(a) and 6(c) for the four RCPs considered in recent IPCC assessment reports [83]. The first three, more moderate ones, only lead up to 290 K by 2100, in the case of RCP 6.0. The most severe one, RCP 8.5, is shown to be unstoppable on the way to the hothouse, past roughly 291 K.

For a fixed amount of annual carbon emissions e , two processes are decisive in the TCV model in determining the transition to a stable hothouse climate. First, the self-sustained darkening of ice sheets and other terrestrial cryosphere components, due to the glacial micro algae growth on their surface [61–63]. While no ice sheets, mountain glaciers or snow cover terrestrial are explicitly represented in our model, this algal-bloom effect is implicitly captured by including it in the formulation of the land albedo α_L as a function of temperature; see equation (M.2') in the Methods section. Second, the degradation of the global ecosystem due to the incremental death of the vegetation that is least tolerant to heat stress, and the subsequent decline in global net ecosystem productivity occurring after an initial increase driven by carbon fertilization effect

encoded by Eq. (S6) [64–66, 87]; see "Impact of temperature stress on land vegetation" in the Methods section.

Figure 6(a) is a three-dimensional regime diagram in the $(T_{\alpha_{L,\ell}}, V, e)$ parameter space: it is divided by a two-dimensional surface that separates the current-climate regime below it from the regime above it, in which a hothouse-like state is the only one that is stable. In the latter regime, global average temperature T is about 10 K higher than the present-climate regime. Videos that follow the changes in the model's phase portrait for $V = 0$ and $V = 0.3$ as e increases can be found in the Supplementary Material.

Figure 6(b) illustrates the boundary (blue solid line) between the current-climate and the hothouse regime for $T_{\alpha_{L,\ell}} = 290$ K. Figure 6(c) shows the evolution of global temperature for the RCP 8.5 emissions scenario. It exhibits a clear increase in slope as the trajectory enters the hothouse world. A video, labeled `TCV_video-V=V(t)`, that illustrates in greater detail the model's behavior in this case is also available in the Supplementary Material. This video is compared there with two videos, labeled `TCV_video-V=0` and `TCV_video-V=0.3`, in which the vegetation degradation index V is kept constant at $V = 0$ and $V = 0.3$, respectively.

The distinction between model behavior in simulations that keep e or V fixed and those that allow the forcing $e(t)$ to evolve as prescribed and the variable $V(t)$ to evolve according to equation (2c) can only be understood fully in the context of the theory of nonautonomous dynamical systems [2, 39]. Such an approach, though, requires further numerical studies that go beyond the framework of the current paper.

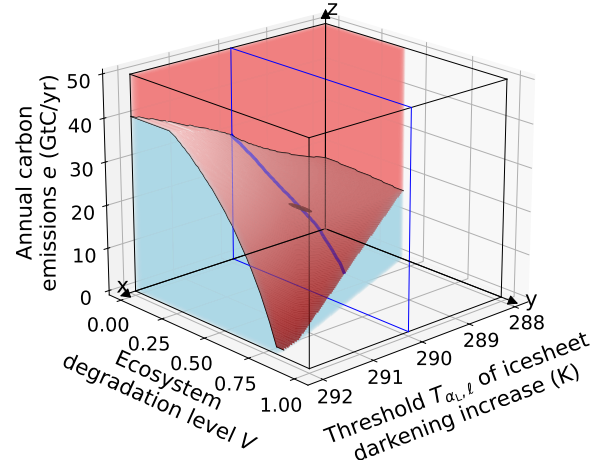
Figure 6 allows one to establish safety margins for annual emissions $e(t)$. When a certain threshold temperature $T_{\alpha_{L,\ell}}$ is attained, algal growth on the surface of the terrestrial cryosphere allowing therewith its darkening becomes self-sustained, leading to the acceleration of the drop of terrestrial albedo (on the x -axis of Fig. 6(a)), while a level of ecosystem degradation V has already occurred (on the figure's y -axis). For illustration purposes, the 2022 level of scenario-based GHG emissions is $e \simeq 11.6$ GtC/yr, while the estimated V equals 0.09.

Assuming a median $T_{\alpha_{L,\ell}} = 290$ K threshold temperature, the buffer distance — i.e., the maximum amount of annual emissions e that can still be emitted without causing a jump to the hothouse state — is of 22.5 GtC/yr. This buffer distance diminishes until reaching less than 1 GtC/yr in 2085 for RCP 8.5. We note that for higher levels of global vegetation degradation, the TCV model does not exhibit bistability for all $(V, T_{\alpha_{L,\ell}})$ -values contained in the orange volume in Fig. 6. Instead, warming accelerates and the global temperature still reaches temperatures comparable to hothouse ones. An accelerated warming is initiated by the onset of darkening of the terrestrial cryosphere.

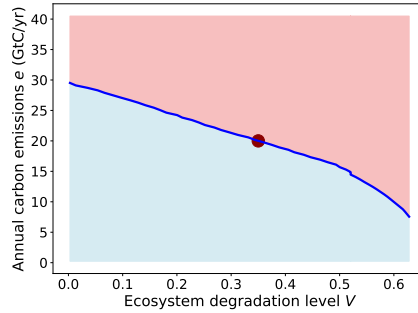
4 Discussion and conclusions

We formulated a 0-D model for the global temperatures T and either two separate (TCV) or a single (TCV-DAE) carbon reservoir stock, i.e., either atmospheric C_A and oceanic mixed layer C_M or combined atmospheric and mixed-layer C_S . A separate equation for the evolution of the ecosystem degradation effect on the system, carried by the variable V , complements those for T and C . The full TCV model appears as the four-ODE system (1), the TCV-DAE one as system (2), with its three ODEs and an algebraic equation that states the fast equilibration of C_A and C_M .

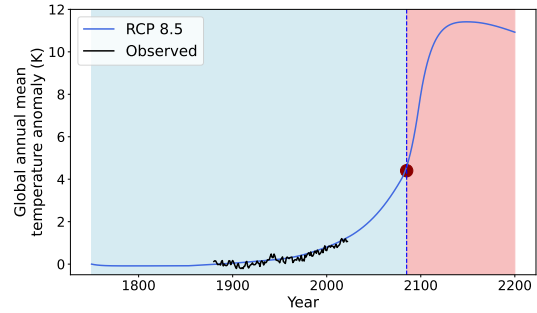
This coupled TCV model is highly idealized but it does include major physical, chemical and biological processes affecting the Earth system. It is based on the system's radiation budget [50, 53, 88], the carbon sink dynamics of the ocean [44, 89] and of the land vegetation [42, 54, 55, 90], and on the radiative forcing by anthropogenic GHGs [58]. The model's parameter values rely on



(a) Regime diagram in the $(T_{\alpha_{L,\ell}}, V, e)$ parameter space



(b) Regime boundary for $T_{\alpha_{L,\ell}} = 290$ K



(c) Temperature evolution under RCP 8.5

Figure 6: **Regime diagram for the TCV model's shift from present climate to hothouse.** (a) Regime diagram in a three-dimensional parameter space. The diagram's axes are (x) the threshold temperature $T_{\alpha_{L,\ell}}$ of darkening increase on the global cryosphere; (y) land vegetation degradation index V ; and (z) annual emissions e . The e values for each $(T_{\alpha_{L,\ell}}, V)$ indicate the threshold of annual emissions beyond which the present climate P_1 will shift to the hothouse P_2 ; see Figs. 3 and Fig. 4. (b) Two-dimensional section of panel (a) at $T_{\alpha_{L,\ell}} = 290$ K; the regime boundary separating in this section the hothouse (red-pink) from the current climate (light blue) steady states is shown in dark blue. (c) Evolution of temperature for the RCP 8.5 emissions scenario, when $V(t)$ evolves according to equation (2c). In both panels (b) and (c), the red-filled circle indicates the occurrence of the TCV model's tipping from the stable P_1 present climate via the unstable P_3 steady state to the P_2 stable hothouse.

an extensive review of the existing literature; see Tables S1, S3, and S2.

Both the full and the reduced model include the ice-albedo feedback and the anthropogenic GHG emissions forcing in the energy balance equation (1a) or (2a), respectively, while the temperature-dependent carbon fluxes between reservoirs are modeled by equations (1b) and (1c) or by (2b), respectively. The two key novelties in our conceptual model are included in the first ODE of both systems (1) and (2), and in the state-of-the-vegetation equations (1d) or (2c), respectively. They are: (i) the inclusion of the biogeophysical feedback between the algal bloom on ice sheets and the

rest of the land cryosphere and the global temperature T , via the reduction of the land albedo α_L due to the darkening of the Earth's cryosphere as shown in Fig. 2, especially at high latitudes, that this bloom produces [61–63, 73]; and (ii) the temperature–vegetation degradation feedback that leads to the land vegetation's die-off as temperatures rise [64–66, 87]. The temperature-albedo feedback included in the TCV model is of $1.1 \text{ W.m}^{-2}.\text{K}^{-1}$ which is consistent with orders of magnitude of temperature-albedo feedback that could be observed at planetary scale on Earth [91]. These two regional processes and feedback value are described further in the Methods section.

The difference between the full TCV and the reduced TCV-DAE model resides in equation (2d), which postulates instantaneous equilibration between the atmospheric and the mixed-layer reservoirs, based on this equilibration being much faster than between the other pairs of reservoirs[60]. The DAE model allowed us to carry out the phase-plane analysis illustrated in Fig. 3, complemented by the bifurcation analysis whose results appear in Fig. 4.

Figure 3 shows clearly that there are three intersections — P_1 , P_2 , and P_3 — of the two nullclines given by $F_1(T, C_S) = 0$ (blue solid line) and $F_2(T, C_S) = 0$ (red solid line), along which the global temperature T and the combined carbon stock C_S in the atmosphere and the ocean mixed layer, respectively, are constant. These intersections correspond to fixed points or steady states of the DAE system (2); an additional, unstable fixed point lies above the area of the phase plane in Fig. 3. The two bifurcation diagrams in Fig. 4 illustrate the dependence of these three fixed points on the anthropogenic GHG emission rate e . The diagram in panel (a) is for $V = 0$, that in (b) is for $V = 0.3$, where V is the degradation level of land vegetation, with $0 \leq V \leq 1$.

In these diagrams, the two bifurcation points occur at the lower-right of the figure — i.e., for positive emission rates $e_c \simeq +31.5 \text{ GtC/yr}$ when $V = 0$ — and further to the left, for lower emission rates, at $e_d = 16.5 \text{ GtC/yr}$ for both $V = 0$ and $V = 0.3$. For positive emission rates, though, degradation V of the vegetation affects quite strongly the point at which the climate will jump from a mildly increased temperature to a hothouse one: it is $e_c = 21.5 \text{ GtC/yr}$ for $V = 0.3$ vs. $e_c \simeq 31.5 \text{ GtC/yr}$ for $V = 0$.

Multistability is ubiquitous in the sciences in general [92] and bistability, in particular, has been established in the climate sciences in the early 1960s [2, 37, 38]; see also Fig. ?? and its discussion in the Supplementary Material. The crucially new result of the present work is that there exists a branch of hothouse solutions, roughly 8 K above the lowermost branch, which corresponds here to the current climate. This stable branch of hothouse steady states does not seem to have been found so far by either conceptual or more detailed models. On the other hand, paleoclimatic evidence of a climate similar to such a hothouse does exist, during the Paleocene-Eocene Thermal Maximum (PETM) [12, 93]. And even the ecosystem deterioration used in our TCV model seems to have manifested itself in the transition to the PETM; see Methods section.

For the highest-emission scenario, RCP 8.5, though, our model exhibits an abrupt tipping to a stable hothouse climate, with the global temperature reaching the value of 299.7 K (26.5 °C); see Fig. 6(c) and the short video `TCV_video-V=V(t)` in the Supplementary Material. The saddle-node bifurcation associated with the collision of the current climate stable steady P_1 with the unstable P_3 state occurs in 2055 when 1,235 GtC of cumulative carbon emissions have been reached in the RCP 8.5 scenario. In comparison, RCP 6.0 has reached 1,073 GtC cumulative emissions. The T - C trajectory of the TCV model diverges from the RCP 8.5 ensemble of IPCC-class ESMs in 2085, when its temperature rises nonlinearly in response to still rising anthropogenic carbon emissions that reach over 28 GtC/yr.

It appears that processes which are regional in nature — like the effect of glacial algal blooms on ice and snow, which is largely confined to high latitudes in both hemispheres, and the differences in resilience of vegetation to temperature increase, which are particularly relevant to the tropics, where temperatures are and will remain the highest — can create pathways of global tipping to a stable

hothouse. These two biogeophysical mechanisms play a major role in facilitating the transition through saddle-node tipping from the current climate to the hothouse state.

Popp *et al.* [18] showed a shift to an unrealistic hothouse steady state about 40 K warmer than preindustrial temperatures using an aquaplanet model initialized at roughly 6 K above present global average temperature. Eisenman & Armour [27] recently obtained a hothouse Earth in a CESM2 GCM simulation at a CO₂ concentration that was 16-fold the present one. However, the change obtained did not occur due to a tipping mechanism but rather as the result of a smooth transition, unlike the tipping that led to a snowball Earth with the same model. It is worth recalling here that 1-D EBMs [34–36] predicted such a snowball Earth long before geochemists found proofs for its occurrence in Earth’s remote past [94], while GCMs were only used for the more detailed investigation of such snowballs after their geochemical documentation [95].

We have shown that the TCV model’s simulations compare quite favorably with instrumental observations for the period 1880–2022, with global temperature and carbon stock evolutions that are barely distinguishable from those of 42 IPCC-class GCMs that participated in CMIP5; see Fig. 1. Moreover, Bland-Altman tests show that — for the 1861–2100 comparison interval used in CMIP5 for evaluating the impact of anthropogenic forcing on global temperatures — the TCV model’s estimates are in close agreement with those of the set of the 42 IPCC-class GCMs. The only noticeable difference between the CMIP5 estimates and the TCV ones occurs at the point at which, for RCP 8.5, the latter undergo a jump to the hothouse climate, while the GCMs – that do not yet include the terrestrial cryosphere darkening mechanism – do not.

References

1. Lenton, T. M., Livina, V. N., Detecting and anticipating climate tipping points & . in *Extreme Events: Observations, Modelling, and Economics* (eds Chavez, M., Ghil, M. & Urrutia-Fucugauchi, J.) 214, 51–62 (AGU - John Wiley & Sons, 2016). ISBN: 978-1-119-15703-8.
2. Ghil, M. & Lucarini, V. The physics of climate variability and climate change. *Reviews of Modern Physics* **92**, 1–77 (2020).
3. Matthews, H. D., Gillett, N. P., Stott, P. A. & Zickfeld, K. The proportionality of global warming to cumulative carbon emissions. *Nature* **459**, 829–832 (2009).
4. Forster, P. *et al.* in (eds Masson-Delmotte, V. P. *et al.*) 923–1054 (Cambridge University Press, Cambridge, United Kingdom and New Yorkd, NY, USA, 2021).
5. Zhu, J., Poulsen, C. J. & Tierney, J. E. Simulation of Eocene extreme warmth and high climate sensitivity through cloud feedbacks. *Science Advances* **5**. ISSN: 2375-2548 (2019).
6. Caballero, R. & Huber, M. State-dependent climate sensitivity in past warm climates and its implications for future climate projections. *Proceedings of the National Academy of Science* **110**, 14162–14167 (2013).
7. Steffen, W. *et al.* Trajectories of the Earth system in the Anthropocene. *Proceedings of the National Academy of Sciences* **115**, 8252–8259 (2018).
8. Aswhin, P. & von der Heydt, A. S. Extreme sensitivity and climate tipping points. *Journal of Statistical Physics* **179**, 1531–1552 (2020).
9. Lenton, T. M. *et al.* Tipping elements in the Earth’s climate system. *Proceedings of the National Academy of Sciences USA* **105**, 1786–1793 (2008).
10. Ghil, M. A century of nonlinearity in the geosciences. *Earth and Space Science* **6**, 1007–1042 (2019).
11. Goldblatt, C. & Watson, A. J. The runaway greenhouse: implications for future climate change, geoengineering and planetary atmonsphere. *Philosophical Transactions of the Royal Society A* **370**, 4197–4216 (2012).
12. Zeebe, R. E. & Zachos, J. C. Long-term legacy of massive carbon input to the Earth system: Anthropocene versus Eocene. *Philosophical Transactions of the Royal Society A: Mathematical, Physical and Engineering Sciences* **371**, 20120006 (2013).
13. Gutjahr, M. *et al.* Very large release of mostly volcanic carbon during the Palaeocene–Eocene Thermal Maximum. *Nature* **548**, 573–577 (2017).
14. Winguth, A. M. E., Shields, C. A. & Winguth, C. Transition into a Hothouse world at the Permian–Triassic boundary—A model study. *Palaeogeography, Palaeoclimatology, Palaeoecology* **440**, 316–327. ISSN: 0031-0182 (Dec. 2015).
15. Sun, Y. *et al.* Lethally hot temperatures during the early Triassic greenhouse. *Science* **338**, 366–370. ISSN: 1095-9203 (Oct. 2012).
16. Von der Heydt, A. S. *et al.* Quantification and interpretation of the climate variability record. *Global and Planetary Change* **197**, 103399. ISSN: 0921-8181 (2021).
17. Ferreira, D., Marshall, J. & Rose, B. Climate Determinism Revisited: Multiple Equilibria in a Complex Climate Model. *Journal of Climate* **24**, 992–1012. ISSN: 0894-8755 (2011).
18. Popp, M., Schmidt, H. & Marotzke, J. Transition to a moist greenhouse with CO₂ and solar forcing. *Nature Communications* **7** (2016).

19. Wunderling, N. *et al.* Climate tipping point interactions and cascades: a review. *Earth System Dynamics* **15**, 41–74. ISSN: 2190-4987 (Jan. 2024).
20. Rising, J., Tedesco, M., Piontek, F. & Stainforth, D. A. The missing risks of climate change. *Nature* **610**, 643–651 (2022).
21. Barnett, M., Brock, W. A. & Hansen, L. P. Pricing uncertainty induced by climate change. *The Review of Financial Studies* **33**, 1024–1066. <http://dx.doi.org/10.2139/ssrn.3008833> (2021).
22. *Handbook of Climate Change Mitigation and Adaptation* 3rd (eds Lackner, M., Sajjadi, B. & Chen, W.-Y.) (Springer Nature, 2022).
23. Palmer, T. & Stevens, B. The scientific challenge of understanding and estimating climate change. *Proceedings of the National Academy of Sciences* **116**, 24390–24395 (2019).
24. Slingo, J. & Palmer, T. M. Uncertainty in weather and climate prediction. *Philosophical Transactions of the Royal Society A* **369**, 4751–4767 (2011).
25. Hall, A., Cox, P., Huntingford, C. & Klein, S. Progressing emergent constraints on future climate change. *Nature Climate Change* **9**, 269–278 (2019).
26. Sherwood, S. C. *et al.* An assessment of Earth’s climate sensitivity using multiple lines of evidence. *Reviews of Geophysics* **58**. ISSN: 1944-9208 (2020).
27. Eisenman, I. & Armour, K. C. The radiative feedback continuum from Snowball Earth to an ice-free hothouse. *Nature Communications* **15**. ISSN: 2041-1723 (2024).
28. Schneider, S. H. & Dickinson, R. E. Climate modelling. *Reviews of Geophysics and Space Physics* **25**, 447–493 (1974).
29. Ghil, M. Hilbert problems for the geosciences in the 21st century. *Nonlinear Processes in Geophysics* **8**, 211–211 (2001).
30. Held, I. M. The gap between simulation and understanding in climate modeling. *Bulletin of the American Meteorological Society* **86**, 1609–1614 (2005).
31. IPCC. *Climate Change 2021: The Physical Science Basis, Working Group I Contribution to the Sixth Assessment Report of the Intergovernmental Panel on Climate Change*, V. Masson-Delmotte, P. Zhai *et al.*, eds. (Cambridge University Press, June 2021).
32. Budyko, M. I. The effect of solar radiation variations on the climate of the Earth. *Tellus* **21**, 611–619 (1969).
33. Sellers, W. D. A global climatic model based on the energy balance of the Earth atmosphere. *Journal of Applied Meteorology* **8**, 392–400 (1969).
34. Held, I. M. & Suarez, M. J. Simple albedo feedback models of the ice caps. *Tellus* **26**, 613–629 (1974).
35. Ghil, M. Climate stability for a Sellers-type model. *Journal of the Atmospheric Sciences* **33**, 3–20 (1976).
36. North, G. R., Cahalan, R. F. & Coakley, J. A. Energy balance climate models. *Reviews of Geophysics and Space Physics* **19**, 19–121 (1981).
37. Stommel, H. Thermohaline convection with two stable regimes of flow. *Tellus* **13**, 224–230 (1961).
38. Lorenz, E. N. Deterministic nonperiodic flow. *Journal of the Atmospheric Sciences* **20**, 130–141 (1963).

39. Boers, N., Ghil, M. & Stocker, T. F. Theoretical and paleoclimatic evidence for abrupt transitions in the Earth system. *Environmental Research Letters* **17**, 093006 (2022).

40. Lenton, T. M. Land and ocean carbon cycle feedback effects on global warming in a simple Earth system model. *Tellus B: Chemical and Physical Meteorology* **52**, 1159–1188 (2000).

41. Friedlingstein, P. Carbon cycle feedbacks and future climate change. *Philosophical Transactions of the Royal Society A* **373**, 1–14 (2015).

42. Svirezhev, Y. M. & von Bloh, W. Climate, vegetation, and global carbon cycle: the simplest zero-dimensional model. *Ecological Modelling* **101**, 79–95 (1997).

43. Anderies, J. M., Carpenter, S. R., Steffen, W. & Rockström, J. The topology of non-linear global carbon dynamics: from tipping points to planetary boundaries. *Environmental Research Letters* **8**, 044048 (2013).

44. Lade, S. J. *et al.* Analytically tractable climate–carbon cycle feedbacks under 21st century anthropogenic forcing. *Earth System Dynamics* **9**, 507–523 (2018).

45. Friedlingstein, P. Carbon cycle feedbacks and future climate change. *Philosophical Transactions of the Royal Society A: Mathematical, Physical and Engineering Sciences* **373**, 20140421 (2015).

46. Hartin, C. A., Patel, P., Schwarber, A., Link, R. P. & Bond-Lamberty, B. P. A simple object-oriented and open-source model for scientific and policy analyses of the global climate system – Hector v1.0. *Geoscientific Model Development* **8**, 939–955. ISSN: 1991-9603 (2015).

47. Smith, C. J. *et al.* FAIR v1.3: a simple emissions-based impulse response and carbon cycle model. *Geoscientific Model Development* **11**, 2273–2297. ISSN: 1991-9603 (2018).

48. Hoffman, P. F., Kaufman, A. J., Halverson, G. P. & Schrag, D. P. A Neoproterozoic Snowball Earth. *Science* **281**, 1342–1346 (1998).

49. Lenton, T. M. *et al.* Climate tipping points - too risky to bet against. *Nature* **575**, 592–595 (2019).

50. Källén, E., Crafoord, C. & Ghil, M. Free oscillations in a climate model with ice-sheet dynamics. *Journal of the Atmospheric Sciences* **36**, 2292–2303 (1979).

51. Hourdin, F. *et al.* The art and science of climate model tuning. *Bulletin of the American Meteorological Society* **98**, 589–602 (2017).

52. Kim, S.-K., Kim, H.-J., Dijkstra, H. A. & An, S.-I. Slow and soft passage through tipping point of the Atlantic Meridional Overturning Circulation in a changing climate. *Climate and Atmospheric Science* **5**. ISSN: 2397-3722 (Feb. 2022).

53. Crafoord, C. & Källén, E. A note on the condition for existence of more than one steady-state solution in Budyko-Sellers type models. *Journal of the Atmospheric Sciences* **35**, 1123–1125 (1978).

54. Potter, C. S. *et al.* Terrestrial ecosystem production: A process model based on global satellite and surface data. *Global Biogeochemical Cycles* **7**, 811–841 (1993).

55. Mahecha, M. D. *et al.* Global convergence in the temperature sensitivity of respiration at ecosystem level. *Science* **329**, 838–840 (2010).

56. Eppley, R. W. Temperature and phytoplankton growth in the sea. *Fishery Bulletin* **70**, 1063–1085 (1972).

57. Henson, S. A., Sanders, R. & Madsen, E. Global patterns in efficiency of particulate organic carbon export and transfer to the deep ocean. *Global Biogeochemical Cycles* **26**, 1–14 (2012).

58. Myhre, G., Highwood, E. J., Shine, K. P. & Stordal, F. New estimates of radiative forcing due to well mixed greenhouse gases. *Geophysical Research Letters* **25**, 21715–2718 (1998).

59. Broecker, W. S. & Peng, T.-H. *Tracers in the Sea* (Lamont-Doherty Geological Observatory, Columbia University, Palisades, New York, 1982).

60. Zeebe, R. E. & Wolf-Gladrow, D. *CO₂ in Seawater: Equilibrium, Kinetics, Isotopes* (Elsevier, 2001).

61. Williamson, C. J. *et al.* Algal photophysiology drives darkening and melt of the Greenland Ice Sheet. *Proceedings of the National Academy of Sciences* **117**, 5694–5705 (2020).

62. Millar, J. L. *et al.* Alpine glacier algal bloom during a record melt year. *Frontiers in Microbiology* **15**. ISSN: 1664-302X (2024).

63. Tedesco, M. *et al.* The darkening of the Greenland ice sheet: trends, drivers, and projections (1981–2100). *The Cryosphere* **10**, 477–496 (2016).

64. Allen, D. A. *et al.* A global overview of drought and heat-induced tree mortality reveals emerging climate change risks for forests. *Forest Ecology and Management* **259**, 660–684 (2010).

65. Xu, H., Xiao, J. & Zhang, Z. Heatwave effects on gross primary production of northern mid-latitude ecosystems. *Environmental Research Letters* **15**, 074027 (2020).

66. Hammond, W. M. *et al.* Global field observations of tree die-off reveal hotter-drought finger-print for Earth's forests. *Nature Communications* **13** (2022).

67. Held, I. M. *et al.* Probing the fast and slow components of global warming by returning abruptly to preindustrial forcing. *Journal of Climate* **23**, 2418–2427 (2010).

68. Pierrehumbert, R. T. Short-lived climate pollution. *Annual Review of Earth and Planetary Science* **42**, 341–379 (2014).

69. Bland, J. M. & Altman, D. G. Measuring agreement in method comparison studies. *Statistical Methods in Medical Research* **8**, 135–160 (1999).

70. Taylor, K. E., Stouffer, R. J. & Meehl, G. A. An Overview of CMIP5 and the Experiment Design. *Bulletin of the American Meteorological Society* **93**, 485–498. ISSN: 1520-0477 (2012).

71. Friedlingstein, P., O'Sullivan, M., Jones, M. W., *et al.* Global Carbon Budget 2022. *Earth System Science Data* **14**, 4811–4900 (2022).

72. Williamson, C. J. *et al.* Glacier algae: A dark past and a darker future. *Frontiers in Microbiology* **10** (2019).

73. Yallop, M. L. *et al.* Photophysiology and albedo-changing potential of the ice algal community on the surface of the Greenland ice sheet. *The ISME Journal* **6**, 2302–2313. ISSN: 1751-7370 (2012).

74. Boone, A. & Etchevers, P. An Intercomparison of Three Snow Schemes of Varying Complexity Coupled to the Same Land Surface Model: Local-Scale Evaluation at an Alpine Site. *Journal of Hydrometeorology* **2**, 374–394. ISSN: 1525-7541 (2001).

75. Boone, A. *Description of the snow framework of the ISBA-ES model* tech. rep. (National Centre for Meteorological Research, Centre National de Recherches Météorologiques, Météo-France 42, avenue G. Coriolis, 31057 Toulouse Cedex France, 2010). 10.1002/2015GL066275http://www.umn-cnrm.fr/IMG/pdf/snowdoc_v2.pdf.

76. Hawkins, E. *et al.* Estimating Changes in Global Temperature since the Preindustrial Period. *Bulletin of the American Meteorological Society* **98**, 1841–1856. ISSN: 1520-0477 (2017).

77. Arnold, V. *Geometric Methods in the Theory of Ordinary Differential Equations* 334 pp. (Springer, New York/Berlin, 1983).

78. Ghil, M. & Childress, S. *Topics in Geophysical Fluid Dynamics: Atmospheric Dynamics, Dynamo Theory, and Climate Dynamics; reprinted as an eBook in 2012* (Springer Science+Business Media, Berlin/Heidelberg, 1987).

79. Guckenheimer, J. & Holmes, P. *Nonlinear Oscillations, Dynamical Systems and Bifurcations of Vector Fields* (Springer-Verlag, Berlin, 1983).

80. Sobol, I. M. Global sensitivity indices for nonlinear mathematical models and their Monte Carlo estimates. *Mathematics and Computers in Simulation* **55**, 271–280. ISSN: 0378-4754 (Feb. 2001).

81. Saltelli, A. *et al.* *Global Sensitivity Analysis. The Primer* ISBN: 9780470725184 (Wiley, 2007).

82. Jansen, M. J. W. Analysis of variance designs for model output. *Computer Physics Communications* **117**, 35–43. ISSN: 0010-4655 (1999).

83. Meinshausen, M. *et al.* The RCP greenhouse gas concentrations and their extinctions from 1765 to 2300. *Climatic Change* **109**, 213–241 (2011).

84. Keeling, C. *et al.* Atmospheric carbon dioxide variations at Mauna Loa Observatory, Hawai. *Tellus* **28**, 538–551 (1976).

85. NOAA. *Climate at a Glance Global Time Series* National Oceanic and Atmospheric Administration. https://www.nci.noaa.gov/access/monitoring/climate-at-a-glance/global/time-series/globe/land_ocean/ytd/12/1850-2022.

86. IIASA. *RCP Database* <http://www.iiasa.ac.at/web-apps/tnt/RcpDb>.

87. Wu, X. & Jiang, D. Probabilistic impacts of compound dry and hot events on global gross primary production. *Environmental Research Letters* **17**, 034049 (2022).

88. Rombouts, J. & Ghil, M. Oscillations in a simple climate-vegetation model. *Nonlinear Processes in Geophysics* **22**, 275–288 (2015).

89. Henson, S. A. *et al.* A reduced estimate of the strength of the ocean's biological carbon pump. *Geophysical Research Letters* **38**, 1–5 (2011).

90. Huang, M. *et al.* Air temperature optima of vegetation productivity across global biomes. *Nature Ecology and Evolution* **3**, 772–779 (2019).

91. Flanner, M. G., Shell, K. M., Barlage, M., Perovich, D. K. & Tschudi, M. A. Radiative forcing and albedo feedback from the Northern Hemisphere cryosphere between 1979 and 2008. *Nature Geoscience* **4**, 151–155. ISSN: 1752-0908 (Jan. 2011).

92. Parisi, G. Nobel Lecture: Multiple Equilibria. *Reviews of Modern Physics* **95**, 1–17 (2023).

93. Turner, S. K., Hull, P. M., Kump, L. R. & Ridgwell, A. A probabilistic assessment of the rapidity of PETM onset. *Nature Communications* **8** (2017).

94. Hoffman, P. & Schrag, D. The snowball Earth hypothesis: testing the limits of global change. *Terra Nova* **14**, 129–155 (2002).

95. Pierrehumbert, R. T. High levels of atmospheric carbon dioxide necessary for the termination of global glaciation. *Nature* **429**, 646 (2004).

Methods

Model

We describe here the physical, chemical and biological processes that enter the formulation of the full TCV model governed by the system (1). Its four ODEs govern the evolution in time of global temperatures T , two carbon stocks, atmospheric C_A and oceanic C_M , and a terrestrial vegetation ecosystem degradation variable V . The reduced DAE version thereof — governed by the system (2), with its three ODEs and an algebraic equation — is based on the same processes, except for the absence of the carbon flux between the atmosphere and the ocean mixed layer, which is set to zero in equation (2d), due to the rapid equilibration between these two reservoirs [60]. Due to this equilibration, C_A and C_M are replaced by their sum, $C_S = C_A + C_M$.

Radiative budget and the TCV model's EBM

Equations (1a) and (2a) are identical to each other, and they represent essentially the model's global-temperature evolution subject to natural radiation balance [53, 78], which is modified by the anthropogenic GHG forcing R_a as the atmospheric carbon C_A increases above the baseline $C_{A,0}$ preindustrial content due to anthropogenic emissions $e(t)$,

$$c\dot{T} = R_i - R_o + R_a. \quad (\text{S1})$$

Here the incoming radiation $R_i = Q_0(1 - p\alpha_L(T) - (1 - p)\alpha_O(T))$ is the product of the solar constant Q_0 and of the planetary albedo α_{pl} [32, 33], to which the land and the ocean surface contribute in the proportion $p : (1 - p)$ [50], where p is the fraction of land. The outgoing radiation R_o is given by a Budyko-style linear function of temperature [32], $R_o = \kappa(T - T_\kappa)$, with $T_\kappa = 154$ K, and c is the heat capacity [96].

The ocean albedo $\alpha_O(T)$ is given by the piecewise-linear ramp function of Sellers [33, 35, 97].

$$\alpha_O(T) = \begin{cases} \alpha_{\text{max}}^O & \text{if } T \leq T_{\alpha_O,\ell}, \\ \alpha_{\text{max}}^O + \frac{\alpha_{\text{min}}^O - \alpha_{\text{max}}^O}{T_{\alpha_O,u} - T_{\alpha_O,\ell}}(T - T_{\alpha_O,\ell}) & \text{if } T_{\alpha_O,\ell} < T \leq T_{\alpha_O,u}, \\ \alpha_{\text{min}}^O & \text{if } T_{\alpha_O,u} < T. \end{cases} \quad (\text{S2})$$

Here $\alpha_{\text{max}}^O = 0.57$ [33, 98] corresponds to a completely sea ice-covered ocean [99, 100] at global temperatures below $T_{\alpha_O,u} = 200$ K, following an authoritative review of Neoproterozoic literature [101], while an ice-free ocean has a top-of-atmosphere albedo of $\alpha_{\text{min}}^O = 0.26$ [33] when the global temperature is higher than $T_{\alpha_O,\ell} = 299$ K. Between 200 K [101] and 299 K [50], the ocean albedo decreases linearly. De Vrese et al. [98] studied snowball Earth [48, 94] climate dynamics to determine plausible albedo values using the MPI-ESM climate model and obtained values of planetary albedos of 0.57–0.7.

Our model's formulation of land albedo $\alpha_L(T)$ is likewise via a piecewise-linear ramp function, with α_O replaced by $\alpha_L(T)$ and distinct tie points at which the derivative of the albedo with respect to temperature is discontinuous. The land albedo decreases from a maximum level $\alpha_{\text{max}}^L = 0.4$ for $T_{\alpha_L,\ell} = 290$ K [74] to a minimum land albedo of $\alpha_{\text{min}}^L = 0.35$ [73, 74] when the global temperature attains $T_{\alpha_L,u} = 294$ K and the cryosphere has been completely darkened as explained below. We shall refer to this land albedo model as equation (M.2').

The global temperature $T_{\alpha_L,\ell}$ corresponds to the temperature of initiation of self-sustained darkening of the icesheets. It is when this threshold temperature is reached that the algal-blooms-covered surface increases year after year, leading to decreasing albedo until a minimum is reached

at $T = T_{\alpha_{L,u}}$. It is at this point, in particular, that a maximum extent of surface of the polar ice sheets and the rest of the terrestrial cryosphere (see Fig. 2), is uniformly darkened by algal blooms and provides a suitable environment for these blooms to develop upon [61, 63]. The value of $T_{\alpha_{L,\ell}} = 290$ K mentioned above is roughly 4 K higher than the present climate and it represents the median of recent estimates for the triggering of self-sustained darkening of major ice sheets [102].

The break point $T_{\alpha_{L,u}} = 294$ K corresponds to a temperature with a maximum surface of terrestrial cryosphere covered in melted ice or snow. At this temperature, we consider the entire midlatitude and mountain glaciers surface as well as the whole Greenland icesheet [103] to be suitable for algal growth. While the surface mass balance over this entire area — i.e., the accumulated mass of snow minus the mass lost through melting — has become negative, in the Antarctica, the ice sheet surface below 2 500 m of altitude¹ is in a melt state [105, 106], while the area above remains fully frozen and with a high albedo level of 0.8.

The two ramp functions used herein are clearly a substantial simplification that is compatible with the overall simplicity of our TCV model. Such simplifications have been used in several 0-D[33] or 1-D[107] EBMs, as well as in fully-fledged 3-D IPCC-class GCMs [108, 109].

Concerning the effect of anthropogenic GHG emissions $e(t)$ in Eq. 1b on R_a , Myhre et al. [58] showed that a logarithmic function captures fairly accurately this effect over the range of CO₂ concentrations currently experienced. Based on their widely applied work, we take $R_a = a \ln(C_A/C_0)$, with a the GHG radiative forcing constant of CO₂; see Table S1.

In order, though, to determine the future evolution of the global temperature T in response to changes in CO₂ levels, we need to account for several feedback mechanisms that, either directly or indirectly, damp or amplify the radiative forcing of GHG gases outside past instrumental ranges.

Biogeophysical feedbacks that affect planetary albedo and the carbon cycle

Two mechanisms play a major role in determining the evolution from the current climate P_1 via the saddle-node bifurcation that causes its tipping to the hothouse state P_2 . The first one refers to rapid changes of albedo, mostly in high latitudes, and it has to do with the effect of algal blooms on the effective albedo of cryospheric components, i.e., ice sheets, sea ice, mountain glaciers and seasonal snow cover. The latter one arises from the differential degradation of land vegetation as temperature rises.

Glacial micro algae darkening of the terrestrial cryosphere

Cryospheric darkening stems from brown-carbon from more frequent forest fires, black-carbon from anthropogenic incomplete combustion, and—above all—the spread of glacier-adapted algae [63]. Field data [110, 111] show this algal effect dominates the darkening-driven rise in surface temperature and melt; satellite analyses reveal a strong inverse ice-sheet-albedo-algal-abundance link [61].

This temperature-amplified algal darkening is poorly represented in state-of-the-art land-surface schemes, yet its impact on the global energy balance must be quantified [72]. We address it with the TCV model, applying algal-bloom darkening only to land. The process starts at $T_{\alpha_{L,\ell}} = 290$ K, reaches its maximum at $T_{\alpha_{L,u}} = 294$ K as shown in Eq. (S3).

¹Elevation data was retrieved from ref. [104]

$$\alpha_L(T) = \begin{cases} \alpha_{\max}^L & \text{if } T \leq T_{\alpha_L, \ell}, \\ \alpha_{\max}^L + \frac{\alpha_{\min}^L - \alpha_{\max}^L}{T_{\alpha_L, u} - T_{\alpha_L, \ell}} (T - T_{\alpha_L, \ell}) & \text{if } T_{\alpha_L, \ell} < T \leq T_{\alpha_L, u}, \\ \alpha_{\min}^L & \text{if } T_{\alpha_L, u} < T. \end{cases} \quad (S3)$$

We do not imply bedrock exposure—complete ice-sheet loss requires centuries–millennia [112, 113]. Rather, reduced surface-mass balance and elevation enlarge the melt area, allowing algae eventually to colonise the whole ice sheet. The chosen $T_{\alpha_L, \ell} = 290$ K lies in the mid-range for self-sustained melting [102, 103, 105, 106, 112, 114, 115], the ramp that drives tipping at (T_c, e_c) .

To derive the drop from α_{\max}^L to α_{\min}^L used in the TCV model (Fig.2), we analysed daily surface-albedo output from a CNRM-CM5 RCP 8.5 run (0.5° grid) that employs the ISBA-ES snow-and-ice module [74, 75]. Focusing on 2070–2100—when $T_{\alpha_L, \ell}$ is reached in IPCC-class models—we computed two gridded daily climatologies: (i) the raw model albedo and (ii) the same fields after resetting every ice- and snow-covered grid cell to the 0.3 albedo of fully algal-covered surfaces [73]. The resulting global annual-mean terrestrial albedos were then obtained as area- and insolation-weighted averages of the gridded means, accounting for latitude-dependent grid size and incoming radiation (Figs.S7a,b) [116]. Global terrestrial albedo thus falls by 0.045 (14 %), giving a temperature-albedo feedback of $pQ_0\Delta\alpha_L/(T_{\alpha_L, u} - T_{\alpha_L, \ell}) = 0.29 \times 342.5 \times 0.045/4 = 1.1 \text{ W m}^{-2} \text{ K}^{-1}$, consistent with observational estimates [91].

Because the TCV model closes the top-of-atmosphere (TOA) energy budget, we add cloud contributions. A mean cloud fraction of 0.47 [117] and the cloud-fraction–albedo relation [118] supply ≈ 0.17 extra albedo units, giving $\alpha_{\max}^L = 0.40$, $\alpha_{\min}^L = 0.35$, and a clear-sky climatological value of 0.23 [119]. Algal darkening of sea-ice—omitted here—would further reduce TOA albedo.

Decrease in the land vegetation’s gross primary productivity (GPP)

Excess stress due to rising temperatures affects numerous physiological functions of land vegetation, which can lead to lowering of carbon uptake and storage capacity and, potentially, to increased mortality [120]. In fact, global temperature increase is known to augment the frequency of occurrence and the extent of vegetation die-offs across both the tropics and subtropics [64, 121–124]. Hammond et al. [66] document the increase of tree mortality across each biome globally in response to conditions of hotter droughts. This phenomenon is also linked to the lowering of vegetation GPP [65, 87, 124, 125]. The reduction of the carbon sink capacity of the global land vegetation as temperatures rise is referred to as the temperature–photosynthesis feedback [126].

Carbon fluxes

Here, we describe the terms entering equations (1b), (1c), and (2b) of the main text.

The land carbon sink

The carbon flux between the atmosphere and the land carbon sink is encoded in $F_{A \rightarrow L}(T, C_A, V)$. The carbon fluxes are certainly not truly Fickian [127], i.e., not linearly proportional to the difference in carbon concentrations. By analogy with nonlinear fluxes in other types of transport, for instance of momentum or heat in a fluid [128], one often assumes such a proportionality and infers from observations or from detailed simulations a coefficient that provides a good approximation to such a proportionality [54].

The flux $F_{A \rightarrow L}(T, C_A, V)$ is equal to the difference between the photosynthetic carbon uptake by the land vegetation's GPP and the release $R_s(T)$ of carbon by soils into the atmosphere through respiration,

$$F_{A \rightarrow L}(T, C_A, V) = P(T, C_A, V) - R_s(T), \quad (S4)$$

where P is the GPP and the difference on the right-hand side of (S4) is also called the Net Primary Productivity (NPP).

We formulated our model for the atmosphere-to-vegetation carbon flux using a carbon simulation model for land vegetation based on the Carnegie-Ames-Stanford approach (CASA)[54] and, in particular, its 0-D version developed by Svirezhev and von Bloh (1997)[42]. The GPP term in the TCV model's equation (1b) is given by

$$P(T, C_A, V) = P_m g_T(T, V) g_C(C_A), \quad (S5)$$

where V is the TCV's level of land vegetation degradation and P_m is the global maximum potential GPP[129].

The multiplicative form of P in (S5) follows Liebig's law of the minimum, also called the limiting-factor paradigm [130]. The factor $g_C(C_A)$ is monotonically increasing functions of the Michaelis–Menten form that saturate at unity, with $g_C(C_A)$ capturing the carbon fertilization effect. Given the still poorly understood impact of elevated CO₂ concentration on the latter effect, we adopt a simple formulation as follows:

$$g_C(C_A) = \frac{C_A}{C_h + C_A}. \quad (S6)$$

Here C_h is half the saturation value of atmospheric carbon concentration, and we use this formula in our own equation (S5). The value of C_h is the half saturation atmospheric carbon concentration of vegetation photosynthetic activity [131]. The carbon fertilization effect encoded by $g_C(C_A)$ is partly responsible for the rise in the flux of carbon from the atmosphere to the land that we observe in our model until 2050 due to the increase of Gross Primary Productivity it drives (see Figs. 5(d) and ??).

The function $g_T(T, V)$ in equation (S5), is chosen to reflect a plateau of global optimum temperatures accounting for all biomes rather than a single global optimum [90], as well as for the impact of the level of degradation of the land vegetation V on P . The precise form of $g_T(T, V)$ is given by

$$g_T(T, V) = \begin{cases} 0 & \text{if } T \leq T_{v,\ell}(V), \\ \frac{T - T_{v,\ell}(V)}{T_{o,\ell}(V) - T_{v,\ell}(V)} & \text{if } T_{v,\ell}(V) < T \leq T_{o,\ell}(V), \\ 1 & \text{if } T_{o,\ell}(V) < T \leq T_{o,u}, \\ \frac{T - T_{v,u}}{T_{v,u} - T_{o,u}} & \text{if } T_{o,u} < T \leq T_{v,u}, \\ 0 & \text{if } T_{v,u} < T. \end{cases} \quad (S7)$$

Simple model of total ecosystem respiration

Soil respiration is the second largest land influx of carbon into the atmosphere [132]; it derives from the respiration of vegetation roots and from the microbial activity of organic matter decomposition in the soils. Considering only soil respiration, annual flux estimations range from 50–75 [133] to 90 [134], or even 108 GtC/year [135] of carbon per year into the atmosphere. Several studies [136–138]

describe the different sources of uncertainty concerning the temperature effect on carbon stored in soils and their implications for ESM-based projections.

In our TCV model we use the classic Q_{10} model [139] to represent temperature-dependent soil respiration as follows:

$$R_s(T) = R_{S,0} Q_{10,S}^{\frac{\Delta T}{10}}; \quad (\text{S8})$$

here $R_{S,0}$ is the preindustrial respiration value at global temperature $T_0 = 286.5$ K[76] and $\Delta T = T - T_0$. This equation is derived from the exponential chemical reaction-temperature R - T rate [139], where $R = R_c Q_{10}^{(T-T_c)/10}$ with R and R_c the reaction rate and baseline rate at T and T_c , respectively, and Q_{10} is the relative increase of the ratio R/R_c for a 10 K temperature increase.

Recent work based on both observational data extracted from the global FLUXNET network and global climate model simulations forced by emission scenarios of increasing severity [140] indicates that the cross-biome spread of Q_{10} values should decrease as global temperature warms converging to a global average of 1.44 in a high emission scenario. This value is also quite close to the global Q_{10} value of 1.5 that we use.

Carbon absorption by the ocean

Diffusion from the atmosphere to the ocean

Following Lade et al.'s (2018)[44] two-box ocean carbon model, we represent the change in carbon stock C_M in the oceanic mixed layer as:

$$\frac{dC_M}{dt} = F_{A \rightarrow M} - F_{M \rightarrow D}. \quad (\text{S9})$$

Here $F_{A \rightarrow M}$ is the flux of carbon from the atmosphere to the mixed layer driven by the gradient of partial pressure p of carbon dioxide, while $F_{M \rightarrow D}$ represents the flux of carbon from the upper ocean to the deep ocean through the solubility and biological pumps.

The equation representing the transport of carbon from the atmosphere to the ocean [44] is:

$$F_{A \rightarrow M} = \frac{DC_{M,0}}{rp(C_{M,0}, 0)} (C_A - p(C_M, \Delta T)), \quad (\text{S10})$$

with ΔT being the global temperature anomaly for the atmosphere and near-surface ocean from preindustrial values, and

$$p(C_M, \Delta T) = C_{A,0} \left(\frac{C_M}{C_{M,0}} \right)^r \frac{1}{1 - D_T \Delta T}. \quad (\text{S11})$$

Here $C_{M,0}$ is the amount stored in the mixed layer at preindustrial equilibrium[141], $C_{A,0}$ is the carbon stock in the atmosphere, and r is the Revelle buffer factor, equal to the ratio of instantaneous change in CO_2 to the change in total dissolved inorganic carbon. Thus, r is a measure of the resistance to atmospheric CO_2 being absorbed at the ocean surface [142, 143]. The CO_2 solubility here is temperature dependent with a factor $D_T = 4.23\% \text{ K}^{-1}$, cf. ref. [144]. We note that the Revelle factor, while kept fixed for simplicity, is projected to increase as anthropogenic carbon emissions rise[145]. The value set by Lade et al that we adopt[44] corresponds to its median value across emission scenarios.

Carbon flux due to overturning flow

Here $F_{M \rightarrow D}^P$ represents the flux of carbon from the oceanic mixed layer to the deeper ocean through the solubility pump, with superscript P for the physical, as opposed to B for the biological pump. We follow Lade et al. [44] in writing

$$F_{M \rightarrow D}^P = w_0(1 - w_T \Delta T)(C_M - C_{M,0}). \quad (S12)$$

Here w_0 represents the rate of exchange of water from the mixed layer to the deep ocean, while w_T is the weakening of the overturning circulation as global temperature T increases.

Temperature-dependent phytoplankton growth

$F_{M \rightarrow D}^B$ is the second component of $F_{M \rightarrow D}$ and represents the flux of carbon from the oceanic mixed layer to the deeper ocean through the biological pump. This flux is determined both by the amount of phytoplankton growth in the surface ocean and by the fraction of that biomass being exported into the deep ocean.

A Q_{10} model is used to encode phytoplankton growth. Eppley[56] used experimental data on a wide range of species of phytoplankton from each of the world's oceans to derive a temperature-dependent maximum growth rate leading to a Q_{10} value of 1.88. However, Eppley-type estimates [56, 146, 147] relate to maximum growth rates. Instead, field estimates of phytoplankton growth rates allow one to derive estimates accounting for nutrient-limited conditions. Sherman et al (2016)[148] report a global Q_{10} value of 1.47 ± 0.08 , based on in situ observations. Based on this, we chose $Q_{10} = 1.5$, as reported in Table S3.

Fraction of phytoplankton transported to the deep ocean

The carbon flux to the deeper ocean through the sinking of organic carbon is captured through the modelling of primary productivity using a Q_{10} -based model [56, 148] and the temperature-dependent fraction of biological carbon exported to the deeper ocean by the biopump. We are interested in the deviation of GPP_{phyto} from the preindustrial equilibrium $GPP_{phyto,0} = p_0$, i.e., we consider $\Delta GPP_{phyto}(T) = p_0 Q_{10}^{\Delta T/10} - p_0$. Three alternative models [89, 149, 150] have been proposed to represent the fraction of biological primary production that is preserved from respiration and recycling in the upper ocean and reaches 100 m depth. However, in order to account for a removal of atmospheric carbon from the upper ocean for a duration of more than 100 years, a depth of over 1,000 m has to be reached by the biopump flux.

We relied, therefore, on unpublished data shared by S. Henson and used in Henson et al (2012) [57] to derive a fraction of phytoplankton primary productivity exported over a depth of 1,000 m or more. This fraction is referred to as $f_H(\Delta T)$ and thus

$$F_{M \rightarrow D}^B(T) = f_H(\Delta T) \Delta GPP_{phyto}(T), \quad (S13)$$

with T in Kelvin, and

$$f_H(\Delta T) = a_{exp} \exp(b_{exp} ((T + 7.15) - 273.15)). \quad (S14)$$

The 7.15 K added to T above represents the sea surface temperature that was used for the measurements yielding these formulas [57]. Here $a_{exp} = 0.0196$ and $b_{exp} = 0.0526$. The dataset in question can be found in ref.[57].

Impact of temperature stress on land vegetation

To reflect the growing evidence of the impact of increased climate stress on land vegetation[64–66], we introduced equation (1d) that describes the degradation of the terrestrial land vegetation. The level V of degradation affects the global-level distribution of vegetation through its effect on Eq. S7 representing the temperature response function $g_T(T, V)$ on of the vegetation productivity.

We repeat below, for the readers' convenience, equation (1d),

$$\dot{V} = (f(T) - \mu V)(1 - V). \quad (\text{S15})$$

The function f captures the global vegetation mortality rate change in response to an increase in global average temperature T and it is defined by

$$f(T) = \begin{cases} 0, & \text{if } \Delta T \leq 0, \\ a_d \Delta T + b_d \Delta T^2, & \text{if } \Delta T > 0, \end{cases} \quad (\text{S16})$$

The nonlinear rise in tree-mortality during hotter droughts is now well established [66, 151], as is the parallel decline in biomass production under combined heat and water stress [152]. A simple quadratic mortality law, $f = f(T)$, with linear and nonlinear coefficients a_d and b_d , respectively, reproduces these responses across vegetation types [153, 154].

With parameters chosen from the species-specific range in [152], the TCV model yields an average disturbance-induced mortality of 0.023 for 2000–2100 under RCP 8.5 (Eq. (S16)). This agrees with the LPJmL Dynamic Global Vegetation Model, which returns 0.02–0.04 for the same scenario, depending on forest type [155].

Cumulative temperature stress, V , evolves toward $\min\{1, f(T)/\mu\}$ and relaxes to zero when $f(T) = 0$, on a timescale μ that represents post-disturbance recovery. Satellite data give $\mu \approx 5\text{--}13$ yr for most biomes [156–158], extending to ≈ 30 yr in boreal forests [159] and > 200 yr in tropical reconstructions [160].

As V increases, vegetation least tolerant to heat is lost and both the lower bound of optimum temperature, $T_{o,\ell}(V)$, and the minimum viable temperature, $T_{v,\ell}(V)$, shift linearly from $T_{o,\ell}^-$, $T_{v,\ell}^-$ to $T_{o,\ell}^+$, $T_{v,\ell}^+$ (Eqs. (S17)–(S18)). Pre-disturbance limits are from [90, 161]. Rising T and V thus drive thermophilization: cold-adapted C₃ species give way to warm-adapted C₄ (and some warm-adapted C₃) vegetation [162]. Accordingly, $T_{v,\ell}^+$ and $T_{o,\ell}^+$ are set to the minimum viable and optimum temperatures of C₄ plants [163, 164].

Figure S1 illustrates the resulting trajectories of $T_{v,\ell}(V)$ and $T_{o,\ell}(V)$ under the three moderate RCP pathways; parameter values are listed in Table S2.

Eqs. (S17) and (S18) below:

$$T_{o,\ell}(V) = \begin{cases} T_{o,\ell}^- & \text{if } V \leq 0, \\ T_{o,\ell}^- + (T_{o,\ell}^+ - T_{o,\ell}^-) V & \text{if } 0 < V \leq 1, \\ T_{o,\ell}^+ & \text{if } 1 < V; \end{cases} \quad (\text{S17})$$

$$T_{v,\ell}(V) = \begin{cases} T_{v,\ell}^- & \text{if } V \leq 0, \\ T_{v,\ell}^- + (T_{v,\ell}^+ - T_{v,\ell}^-) V & \text{if } 0 < V \leq 1, \\ T_{v,\ell}^+ & \text{if } 1 < V. \end{cases} \quad (\text{S18})$$

Figure S1 displays the evolutions of $T_{v,\ell}(V)$ and $T_{o,\ell}(V)$ subject to the three more moderate RCP emission scenarios, as well as their dependence on global temperatures T . Parameter values are given in Table S2.

Reduction of the TCV model to the TCV-DAE model

To reduce our TCV model governed by the four-ODE system (1) to the TCV-DAE model governed by the mixed, differential-and-algebraic equation system (2), we first introduce a variable C_S that accounts for the total amount of carbon in the atmosphere as well as for the dissolved inorganic carbon in the upper ocean, with $C_S = C_A + C_M$. The evolution of C_S satisfies

$$\dot{C}_S = \dot{C}_A + \dot{C}_M = -F_{A \rightarrow L}(T, C_A, V) - F_{M \rightarrow D}^P(T) - F_{M \rightarrow D}^B(T) + e(t). \quad (\text{S19})$$

Defining this new variable leads to a system of ODEs for T , C_S and either C_A or C_M that is equivalent to the original one. In order to reduce this system, we make the assumption that there is fast equilibration between the atmospheric carbon and the mixed-layer carbon [60], i.e. $F_{A \rightarrow M} = 0$ in equation (S10). Using this assumption, equation (S11) yields $C_A = C_{A,0} (C_M/C_{M,0})^r 1/(1 - D_T \Delta T)$ which leads to $C_S = C_A + C_M = C_{A,0} (C_M/C_{M,0})^r 1/(1 - D_T \Delta T) + C_M$.

The latter equation provides an implicit definition of C_M , and hence of C_A , as a function of C_S . Over the range of temperatures and carbon stocks we are looking at, the relationship between C_M and C_S is a smooth one-to-one function, say $C_M = \mathcal{F}(C_S)$. In principle, one could invert the relation and write $C_M = \mathcal{F}^{-1}(C_S) = \mathcal{G}(C_S)$, plug $\mathcal{G}(C_S)$ into system (1) and reduce it therewith to three standard ODEs for T , C_S and V . This means that the stability of the steady states can be computed numerically just as one would for an ODE system, keeping in mind the definition of C_M .

In practice, however, this inversion can only be carried out analytically for $r = 1$ or $r = 2$, i.e., when $\mathcal{F}(C_S)$ is a linear or a quadratic function. Even for $r = 3$ and $r = 4$, it is well known that analytic solutions exist but are too complicated to be useful in actual calculations. Table S3 shows that r is both larger than 4 and fractional, so that we cannot, in general, write C_M explicitly as a function of C_S . Therefore, we consider the system formally as a DAE in Eq. (2). For constant V , this becomes a system of two ODEs and one algebraic equation, which is used for the phase-plane studies in the main text.

Code availability

The code and data used to produce the numerical results and figures is available online on a Zenodo repository.

References

96. Schwartz, S. E. Heat capacity, time constant, and sensitivity of Earth's climate system. *Journal of Geophysical Research* **112**, 1–12 (2007).
97. Zaliapin, I. & Ghil, M. Another look at climate sensitivity. *Nonlinear Processes in Geophysics* **17**, 113–122 (2010).
98. Vrese, P., Stacke, T., Caves J. and Goodman, J. & Brovkin, V. Snowfall-albedo feedbacks could have led to deglaciation of snowball Earth starting from mid-latitudes. *Communications Earth and Environment* **2**. ISSN: 2662-4435 (2021).
99. NSIDC. Sea Ice National Snow and Ice Data Centre. <https://nsidc.org/learn/parts-cryosphere/sea-ice/science-sea-ice>.
100. Pistone, K., Eisenman, I. & Ramanathan, V. Observational determination of albedo decrease caused by vanishing Arctic sea ice. *Proceedings of the National Academy of Sciences* **111**, 3322–3326. ISSN: 1091-6490 (2014).

101. Pierrehumbert, R. T., Abbot, D. S., Voigt, A. & Koll, D. Climate of the Neoproterozoic. *Annual Review of Earth and Planetary Sciences* **39**, 417–460. ISSN: 1545-4495 (2011).
102. Armstrong McKay, D. I. *et al.* Exceeding 1.5 deg C global warming could trigger multiple climate tipping points. *Science* **377** (2022).
103. Box, J. E. *et al.* Greenland ice sheet albedo feedback: thermodynamics and atmospheric drivers. *The Cryosphere* **6**, 821–839. ISSN: 1994-0424 (2012).
104. Danielson, J. & Gesch, D. *Global multi-resolution terrain elevation data 2010 (GMTED2010)* Open-File Report 2011-1073 (U.S. Geological Survey, 2011).
105. Garbe, J., Albrecht, T., Levermann, A., Donges, J. F. & Winkelmann, R. The hysteresis of the Antarctic Ice Sheet. *Nature* **585**, 538–544. ISSN: 1476-4687 (2020).
106. Garbe, J., Zeitz, M., Krebs-Kanzow, U. & Winkelmann, R. The evolution of future Antarctic surface melt using PISM-dEBM-simple. *The Cryosphere* **17**, 4571–4599. ISSN: 1994-0424 (2023).
107. Le Treut, H. & Ghil, M. Orbital forcing, climatic interaction, and glaciation cycles. *Journal of Geophysical Research Oceans* **88**, 5167–5190 (1983).
108. Madsen, M. S. *et al.* The role of an interactive Greenland ice sheet in the coupled climate-ice sheet model EC-Earth-PISM. *Climate Dynamics* **59**, 1189–1211. ISSN: 1432-0894 (2022).
109. Winkelmann, R. *et al.* The Potsdam Parallel Ice Sheet Model (PISM-PIK) – Part 1: Model description. *The Cryosphere* **5**, 715–726. ISSN: 1994-0424 (2011).
110. Cook, J. M. *et al.* Quantifying bioalbedo: a new physically based model and discussion of empirical methods for characterising biological influence on ice and snow albedo. *The Cryosphere* **11**, 2611–2632 (2017).
111. Stibal, M. *et al.* Algae drive enhanced darkening of bare ice on the Greenland Ice Sheet. *Geophysical Research Letters* **44** (2017).
112. Robinson, A., Calov, R. & Ganopolski, A. Multistability and critical thresholds of the Greenland ice sheet. *Nature Climate Change* **2**, 429–432 (2012).
113. Bochow, N. *et al.* Overshooting the critical threshold for the Greenland ice sheet. *Nature* **622**, 528–536 (2023).
114. Boers, N. & Rypdal, M. Critical slowing down suggests that the western Greenland Ice Sheet is close to a tipping point. *Proceedings of the National Academy of Sciences* **118** (2021).
115. Noël, B., van Kampenhout, L., Lenaerts, J. T. M., van de Berg, W. J. & van den Broeke, M. R. A 21st Century Warming Threshold for Sustained Greenland Ice Sheet Mass Loss. *Geophysical Research Letters* **48** (2021).
116. Kopp, G. Daily solar flux as a function of latitude and time. *Solar Energy* **249**, 250–254 (2023).
117. Dutta, S. *et al.* The Reduction in Near-Global Cloud Cover After Correcting for Biases Caused by Finite Resolution Measurements. *Geophysical Research Letters* **47**. ISSN: 1944-8007 (2020).
118. Feingold, G. *et al.* Analysis of albedo versus cloud fraction relationships in liquid water clouds using heuristic models and large eddy simulation. *Journal of Geophysical Research: Atmospheres* **122**, 7086–7102. ISSN: 2169-8996 (2017).

119. Jia, A., Wang, D., Liang, S., Peng, J. & Yu, Y. Global Daily Actual and Snow-Free Blue-Sky Land Surface Albedo Climatology From 20-Year MODIS Products. *Journal of Geophysical Research: Atmospheres* **127**. ISSN: 2169-8996 (2022).

120. Teskey, R. *et al.* Responses of tree species to heat waves and extreme heat events. *Plant, Cell and Environment* **38**, 1699–1712 (2014).

121. Williams, A. P. *et al.* Temperature as a potential driver of regional forest drought stress and tree mortality. *Nature Climate Change* **3**, 292–297 (2012).

122. Van Mantgem, P. J. *et al.* Widespread increase of tree mortality rates in the Western United States. *Science* **323**, 521–524 (2009).

123. Phillips, O. L. *et al.* Drought sensitivity of the Amazon rainforest. *Science* **323**, 1344–1347 (2009).

124. Zhao, M. & Running, S. W. Drought-induced reduction in global terrestrial net primary production from 2000 through 2009. *Science* **329**, 940–943 (2010).

125. Au, J. *et al.* Forest productivity recovery or collapse? Model-data integration insights on drought-induced tipping points. *Global Change Biology* **29**, 5652–5665 (2023).

126. Ciais, P. *et al.* Europe-wide reduction in primary productivity caused by the heat and drought in 2003. *Nature* **437**, 529–533 (2005).

127. Fick, A. Ueber Diffusion. *Annalen der Physik* **170**, 59–86 (1855).

128. Cushman-Roisin, B. & Beckers, J.-M. *Introduction to Geophysical Fluid Dynamics: Physical and Numerical Aspects* (2nd ed.) (Academic Press, 2011).

129. Myneni, R. B., Los, S. O. & Asrar, G. Potential gross primary productivity of terrestrial vegetation from 1982–1990. *Geophysical Research Letters* **22**, 2617–2620. ISSN: 1944-8007 (1995).

130. Sinclair, T. R. Limits to crop yield? *Physiology and determination of crop yield*, 509–532 (1994).

131. Haverd, V. *et al.* Higher than expected CO₂ fertilization inferred from leaf to global observations. *Global Change Biology* **26**, 2390–2402. ISSN: 1365-2486 (2020).

132. Prentice, I. C. e. a. *Climate Change 2001: The Scientific Basis* (Cambridge University Press, 2001).

133. Crowther, T. W. *et al.* Biotic interactions mediate soil microbial feedbacks to climate change. *Proceedings of the National Academy of Sciences* **112**, 7033–7038 (2015).

134. Hashimoto, S. *et al.* Global spatiotemporal distribution of soil respiration modeled using a global database. *Biogeosciences* **12**, 4121–4132 (2015).

135. Hursh, A. *et al.* The sensitivity of soil respiration to soil temperature, moisture, and carbon supply at the global scale. *Global Change Biology* **23**, 2090–2103 (2016).

136. Davidson, E. A. & Janssens, I. A. Temperature sensitivity of soil carbon decomposition and feedbacks to climate change. *Nature* **440**, 165–173 (2006).

137. Warner, D. L., Bond-Lamberty, B., Jian, J., Stell, E. & Vargas, R. Spatial Predictions and Associated Uncertainty of Annual Soil Respiration at the Global Scale. *Global Biogeochemical Cycles* **33**, 1733–1745 (2019).

138. Huntingford, C. *et al.* Implications of improved representations of plant respiration in a changing climate. *Nature Communications* **8** (2017).

139. Van't Hoff, J. H. *Lectures on Theoretical and Physical Chemistry. Part 1: Chemical Dynamics* (ed translated by Lehfeldt, R. A.) (Edward Arnold, 1898).

140. Niu, B. *et al.* Warming homogenizes apparent temperature sensitivity of ecosystem respiration. *Science Advances* **7** (2021).

141. Sarmiento, J. L. & Gruber, N. Sinks for anthropogenic carbon. *Physics Today* **55**, 30–36 (2002).

142. Sabine, C. L. *et al.* The Oceanic Sink for Anthropogenic CO₂. *Science* **305**, 367–371 (2004).

143. Goodwin, P., Williams, R. G., Follows, M. J. & Dutkiewicz, S. Ocean-atmosphere partitioning of anthropogenic carbon dioxide on centennial timescales. *Global Biogeochemical Cycles* **21** (2007).

144. Takahashi, T., Olafsson, J., Goddard, J. G., Chipman, D. W. & Sutherland, S. C. Seasonal variation of CO₂ and nutrients in the high-latitude surface oceans: A comparative study. *Global Biogeochemical Cycles* **7**, 843–878 (1993).

145. Jiang, L.-Q., Carter, B. R., Feely, R. A., Lauvset, S. K. & Olsen, A. Surface ocean pH and buffer capacity: past, present and future. *Scientific Reports* **9**. ISSN: 2045-2322 (2019).

146. Bissinger, J. E., Montagnes, D. J. S., Harples, J. & Atkinson, D. Predicting marine phytoplankton maximum growth rates from temperature: Improving on the Eppley curve using quantile regression. *Limnology and Oceanography* **53**, 487–493 (2008).

147. Regaudie-de-Gioux, A. & Duarte, C. M. Temperature dependence of planktonic metabolism in the ocean. *Global Biogeochemical Cycles* **26**, 1–10 (2012).

148. Sherman, E., Moore, J. K., Primeau, F. & Tanouye, D. Temperature influence on phytoplankton community growth rates. *Global Biogeochemical Cycles* **30**, 550–559 (2016).

149. Laws, E. A., Falkowski, P. G., Smith, W. O., Ducklow, H. & McCarthy, J. J. Temperature effects on export production in the open ocean. *Global Biochemical Cycles* **14**, 1231–1246 (2000).

150. Dunne, J. P., Armstrong, R. A., Gnanadesikan, A. & Sarmiento, J. L. Empirical and mechanistic models for the particle export ratio. *Global Biogeochemical Cycles* **19**, 1–16 (2005).

151. Hartmann, H. *et al.* Research frontiers for improving our understanding of drought-induced tree and forest mortality. *New Phytologist* **218**, 15–28. ISSN: 1469-8137 (2018).

152. Ruiz-Benito, P. *et al.* Stand Structure and Recent Climate Change Constrain Stand Basal Area Change in European Forests: A Comparison Across Boreal, Temperate, and Mediterranean Biomes. *Ecosystems* **17**, 1439–1454. ISSN: 1435-0629 (2014).

153. Lobell, D. B., Bänziger, M., Magorokosho, C. & Vivek, B. Nonlinear heat effects on African maize as evidenced by historical yield trials. *Nature Climate Change* **1**, 42–45. ISSN: 1758-6798 (2011).

154. Ruiz-Benito, P., Lines, E. R., Gómez-Aparicio, L., Zavala, M. A. & Coomes, D. A. Patterns and Drivers of Tree Mortality in Iberian Forests: Climatic Effects Are Modified by Competition. *PLoS ONE* **8** (ed Hector, A.) e56843. ISSN: 1932-6203 (2013).

155. Pugh, T. A. M. *et al.* Understanding the uncertainty in global forest carbon turnover. *Biogeosciences* **17**, 3961–3989. ISSN: 1726-4189 (2020).

156. Bartels, S. F., Chen, H. Y. H., Wulder, M. A. & White, J. C. Trends in post-disturbance recovery rates of Canada's forests following wildfire and harvest. *Forest Ecology and Management* **361**, 194–207 (2016).

157. Goetz, S. J., Fiske, G. J. & Bunn, A. G. Using satellite time-series data sets to analyze fire disturbance and forest recovery across Canada. *Remote Sensing of Environment* **101**, 352–365 (2006).
158. Cuevas-Gonzalez, M., Gerard, F., Balzter, H. & Riano, D. Analysing forest recovery after wildfire disturbance in boreal Siberia using remotely sensed vegetation indices. *Global Change Biology* **15**, 561–577 (2009).
159. Dobor, L. *et al.* Post-disturbance recovery of forest carbon in a temperate forest landscape under climate change. *Agricultural and Forest Meteorology* **263**, 308–322 (2018).
160. Cole, L. E. S., Bhagwat, S. A. & Willis, K. J. Recovery and resilience of tropical forests after disturbance. *Nature Communications* **5** (2014).
161. Lancaster, L. T. & Humphreys, A. M. Global variation in the thermal tolerances of plants. *Proceedings of the National Academy of Sciences* **117**, 13580–13587. ISSN: 1091-6490 (2020).
162. Nolan, C. *et al.* Past and future global transformation of terrestrial ecosystems under climate change. *Science* **361**, 920–923. ISSN: 1095-9203 (2018).
163. Sage, R. F., Wedin, D. A. & Li, M. in (eds Sage, R. F. & Monson, R. K.) 313–356 (Academic Press, 525 B Street, Suite 1900, San Diego, California 92101-4495, USA, 1999). ISBN: 0-12-614440-0.
164. Still, C. J., Berry, J. A., Collatz, G. J. & DeFries, R. S. Global distribution of C3 and C4 vegetation: Carbon cycle implications. *Global Biogeochemical Cycles* **17**. ISSN: 1944-9224 (2003).

Acknowledgements

It is a pleasure to thank William A. Brock for criticism of earlier versions of this manuscript. The authors are grateful to Stephanie Henson for sharing observational data on the fraction of phytoplankton export to the deep ocean, Lester Kwiatkowski for discussions on phytoplankton dynamics, Steven Lade for suggestions on zero-dimensional feedback process modelling, Colin Prentice for comments on the dynamics of land vegetation, Ailsa Roell for editorial comments, Christopher J. Williamson for discussing glacial algal blooms, Philipp de Vrese for sharing MPI-ESM snowball Earth output simulation datasets, Raymond Pierrehumbert for discussing with us plausible values of snowball Earth parameters, Paloma Ruiz Benito for discussing the use and interpretation of empirical vegetation death parameters, and Julius Garbe for discussing the dynamics of surface melting on the Antarctic ice sheet. This is TiPES contribution #280 and ClimTip contribution # $[X'Y'Z']$; the Tipping Points in the Earth System (TiPES) and the Quantifying climate tipping points and their impacts (ClimTip) projects have received funding from the European Union's Horizon research and innovation programme under grant agreements No. 820970 and No. 101137601, respectively. We are grateful to Franklin Allen and the Brevan Howard Centre for Financial Analysis of Imperial College London for support provided. We are grateful also to the Singapore Green Finance Centre for support provided. M.G. also received support from the French Agence Nationale pour la Recherche (ANR) project TeMPlex under grant award ANR-23-CE56-0002.

Supplementary Material

Model parameters

Table S1: Temperature equation parameters

Symbol	Name	Reference value	Value used	Source	Equation
c	Heat capacity	14 ± 6 W·yr·m ⁻² ·K ⁻¹	10 W·yr·m ⁻² ·K ⁻¹	Schwartz [96]	Eq. (1a)
Q_0	Incoming radiation	342.5 W·m ⁻²	342.5 W·m ⁻²	Källén et al. [50]	Eq. (1a)
p	Fraction of land on the planet	0.29	0.29	Källén et al. [50]	Eq. (1a)
α_{\min}^L	TOA land albedo lower bound	0.36	0.36	Boone et al. [75]; Yallop et al. [73]	Eq. (S2)
α_{\max}^L	TOA land albedo upper bound	0.4	0.4	Boone et al. [75]	Eq. (S2)
$T_{\alpha_L,\ell}$	Land albedo lower bound temperature	290.5 K	290.5 K	Robinson et al [112]	Eq. (S2)
$T_{\alpha_L,u}$	Land albedo upper bound temperature	294 K	294 K	Garbe et al [105], Box et al [103]	Eq. (S2)
$T_{\alpha_O,\ell}$	Ocean albedo lower bound temperature	200 K	200 K	Pierrehumbert et al. [101]	Eq. (S2)
$T_{\alpha_O,u}$	Ocean albedo upper bound temperature	299 K	299 K	Källén et al. [50]	Eq. (S2)
α_{\min}^O	TOA ocean albedo lower bound	0.25	0.26	Källén et al. [50]	Eq. (S2)
α_{\max}^O	TOA ocean albedo upper bound	0.55 – 0.7	0.57	De Vrese et al [98]	Eq. (S2)
κ	Temperature linearization parameter	1.74	1.74	Källén et al. [50]	Eq. (1a)
T_κ	Outgoing radiation linearization temperature	154 K	154 K	Källén et al. [50]	Eq. (1a)
a	CO ₂ radiative forcing	5.35 W·m ⁻²	5.35 W·m ⁻²	Myhre et al. [58]	Eq. (1a)
C_0	Reference atmospheric carbon content	590 GtC	610 GtC	Sarmiento and Gruber [141]	Eq. (1a)
T_0	Average equilibrium temperature with no anthropogenic carbon emissions	286.58 K	286.5 K	Hawkins et al [76]	Eq. (1a)

Table S2: **Land carbon sink parameters**

Symbol	Name	Reference value	Value used	Source	Equation
P_m	Potential maximum annual GPP	179.9 GtC/yr	179 GtC/yr	Myneni and Los [129]	Eq. (S5)
C_h	Half saturation carbon atmospheric content	1044 GtC [964–1,131]	1015 GtC	Haverd et al [131]	Eq. (S6)
$R_{L,0}$	Reference land respiration rate	60 GtC/yr	60 GtC/yr	Sarmiento and Gruber [141]	Eq. (S8)
$Q_{10,r}$	Q_{10} factor of the global land respiration	1.5	1.5	Bond-Lamberty and Thomson [0]	Eq. (S8)
$T_{v,\ell}^-$	Lower vegetation viable temperature	257.75 ± 17.4 K	257 K	Lancaster and Humphreys [161]	Eq. (S18)
$T_{v,u}$	Upper vegetation viable temperature	324.45 ± 5.8 K	324 K	Lancaster and Humphreys [161]	Eq. (S18)
$T_{o,\ell}^+$	Upper minimum optimum vegetation temperature	298.15 K	298 K	Still et al [164]	Eq. (S17)
$T_{o,\ell}^-$	Lower minimum optimum vegetation temperature	290.15 K	290.15 K	Huang et al. [90]	Eq. (S17)
$T_{v,\ell}^+$	Upper minimum viable vegetation temperature	288.15 K	289 K	Sage et al [163]	Eq. (S17)
$T_{o,u}$	Lower maximum optimum vegetation temperature	302.15 K	302.15 K	Huang et al. [90]	Eq. (S17)
e	Anthropogenic CO ₂ emissions	–	– GtC	IIASA [86]	Eq. (1b)
a_d	Linear mortality temperature response	$[-0.5, 0.9]$ K ⁻¹	0.006K ⁻¹	Ruiz-Benito et al [154]	Eq. (S15)
b_d	Nonlinear quadratic temperature response	$[-0.6, 0.11]$ K ⁻²	0.0015 K ⁻²	Ruiz-Benito et al [154]	Eq. (S15)
μ	Land vegetation regeneration time	30 yrs	35 yrs	Dobor et al. [159]	Eq. (1d)

Table S3: Ocean carbon sink parameters

Symbol	Name	Reference value	Value used	Source	Equation
D_T	Solubility temperature effect	0.0423 K^{-1}	0.0423 K^{-1}	Takahashi et al. [144]	Eq. (S11)
r	Revelle buffer factor	12.5	12.5	Lade et al. [44]	Eq. (S11)
D	Atmosphere-ocean CO_2 equilibration time	1 yr.^{-1}	1 yr.^{-1}	Lade et al. [44]	Eq. (S11)
$Q_{10,\text{phyto}}$	Q_{10} value of phytoplankton carbon assimilation	1.5	1.5	Sherman et al. [148]	Eq. (S13)
p_0	Reference phytoplankton GPP	50 GtC/yr	50 GtC/yr	Sarmiento and Gruber [141]	Eq. (S13)
w_0	Dissolved inorganic carbon flux rate from the mixed layer to the deep ocean	0.1 yr^{-1}	0.1 yr^{-1}	Lade et al. [44]	Eq. (S12)
w_T	Weakening of the overturning circulation with temperature	0.1 K^{-1}	0.1 K^{-1}	Lade et al. [44]	Eq. (S12)
a_{exp}	Fraction of phytoplankton GPP export below 1,000 meters	0.0196	0.0196	Henson et al. [57]	Eq. (S13)
b_{exp}	Fraction of phytoplankton GPP export below 1,000 meters per degree increase	0.0526 K^{-1}	0.0526 K^{-1}	Henson et al. [57]	Eq. (S13)
$C_{\text{M},0}$	Reference carbon stock in the mixed layer	900 GtC	890 GtC	Sarmiento and Gruber [141]	Eq. (S11)

Evolution of temperatures that affect land vegetation productivity

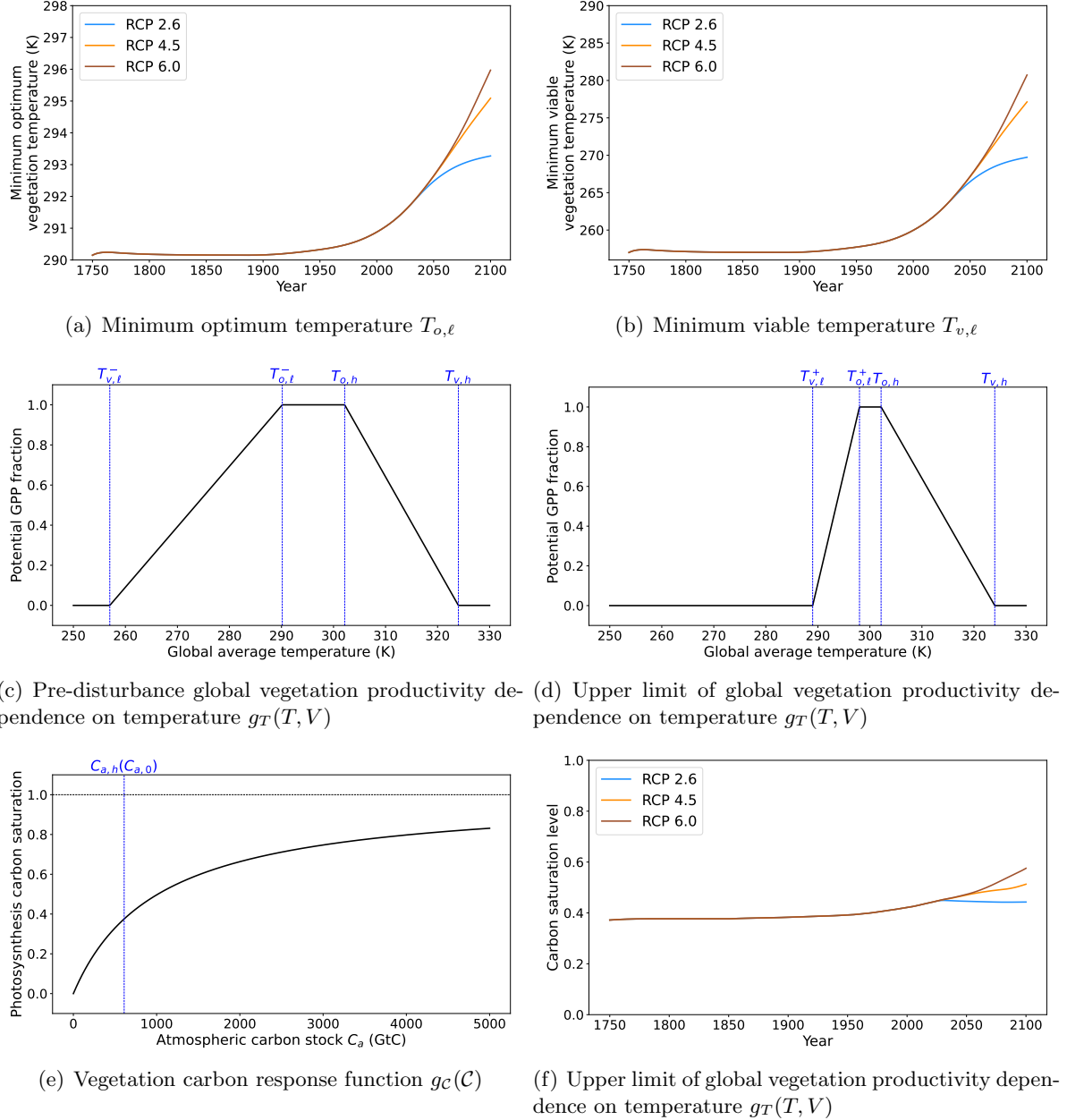


Figure S1: **Evolution of the lower optimum and viable temperatures $T_{o,\ell}$ and $T_{v,\ell}$ and of carbon saturation level $g_C(C)$ for vegetation;** (a, b) evolution of $T_{o,\ell}$ and $T_{v,\ell}$ simulated with the TCV-DAE model subject to the four RCPs 2.6, 4.5, and 6.0; (c) global-ecosystem response $g_T(T, V)$ of vegetation productivity to global temperature T for global ecosystem degradation $V = 0$; (d) global-ecosystem response $g_T(T, V)$ of vegetation productivity to global temperature T for global ecosystem degradation $V = 1$; (e) displays the carbon response function of the global vegetation $g_C(C)$ see Eq. S6 and Table S2. $C_{A,h}$ represents the preindustrial carbon atmosphere content; and (e) Evolution of $g_C(C)$ subject to three moderate RCPs: RCP 2.6, RCP 4.5, and RCP 6.0. Parameter values that label the vertical dash-dotted lines in panels (c), (d), and (e) are presented in Table S2.

TCV model evaluation

TCV temperatures vs. high-end models

We rely here on the Bland-Altman methodology [69] to compare the reliability of temperature estimates using our TCV model versus instrumental observations, on the one hand, and the ensemble mean of 42 GCMs used in CMIP5 [70], on the other. This methodology was devised in the biomedical context and it appears to be new in the climate sciences; hence we indicate briefly the essence thereof. Unlike the RMSE statistic that provides a single aggregate error metric, this test characterises biases and how differences vary across the whole range of values.

Given two sets of measurements, $S_1 = \{s_k^{(1)} : k = 1, 2, \dots, n\}$ and $S_2 = \{s_k^{(2)} : k = 1, 2, \dots, n\}$ of the same n terms of a sequence $S_0 = \{s_k^{(0)} : k = 1, 2, \dots, n\}$, we plot for each index k the mean $x_k = (s_k^{(1)} + s_k^{(2)})/2$ of the two separate measurements and their difference $y_k = s_k^{(1)} - s_k^{(2)}$ in a cartesian (x, y) plot. In the clinical context, the two measurements are typically the results of two different instruments or two distinct measurement techniques. Here, they are estimates of a given climate variable, like global temperature, by the TCV model and by one of the 42 GCMs.

One defines the mean \bar{s} of the entire sample, i.e., the sum of the x_k 's, represented in each panel of Fig. S2 by the dashed blue line, and studies the scatter of the differences y_k . The dotted red lines in the panels indicate, respectively, the values $\bar{s} \pm 1.96\sigma$, which bracket the 95 % confidence interval for a Gaussian scatter. We conclude that the TCV model's estimates are statistically indistinguishable from those of the set of the 42 IPCC-class GCMs.

Visually, the test allows to compare the differences between TCV model and ensemble mean. We analyse firstly the bias of the TCV model with respect to the median of observations and also to the GCM ensemble median. The test allows to visualize the 97.5th percentile of differences and the 2.5th percentile of differences in two horizontal lines – the space between these two lines describes the range within which the central 95 % of the measured differences lie and allow to visualize the difference between the TCV model and the benchmark of comparison across temperature anomaly values. Test results show that TCV model estimates are consistently positioned between these two lines across all tested RCP scenarios (not shown here).

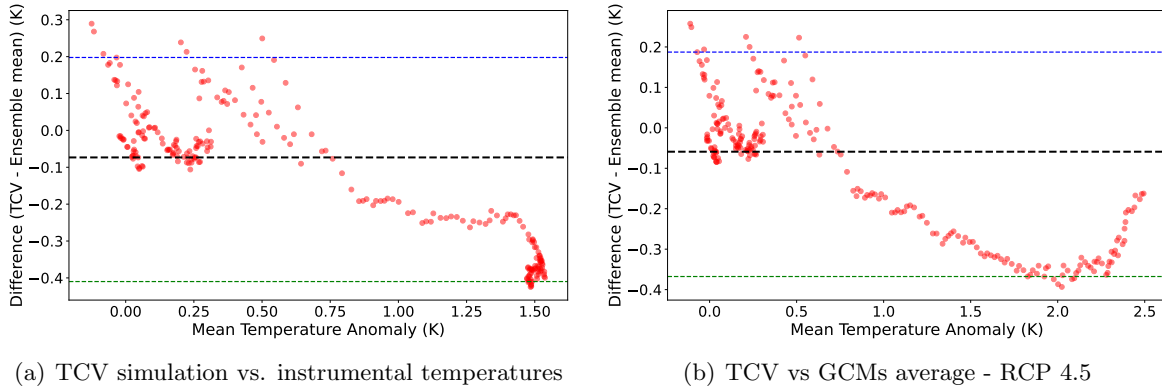


Figure S2: **Bland-Altman non-parametric test plots comparing TCV temperature simulations to observations and to GCM ensemble median.** The red dots display the differences between TCV model and ensemble mean. The heavy dashed black line displays the bias of the TCV model with respect to the median of observations in (a) and to the GCM ensemble median in (b). The light blue dashed lines mark the 97.5th percentile of differences and the dashed green line mark the 2.5th percentile of differences – the space between these two dashed lines describes the range within which the central 95 % of the measured differences lie and allow to visualize the difference between the TCV model and the benchmark of comparison across temperature anomaly values.

Carbon dynamics and validation

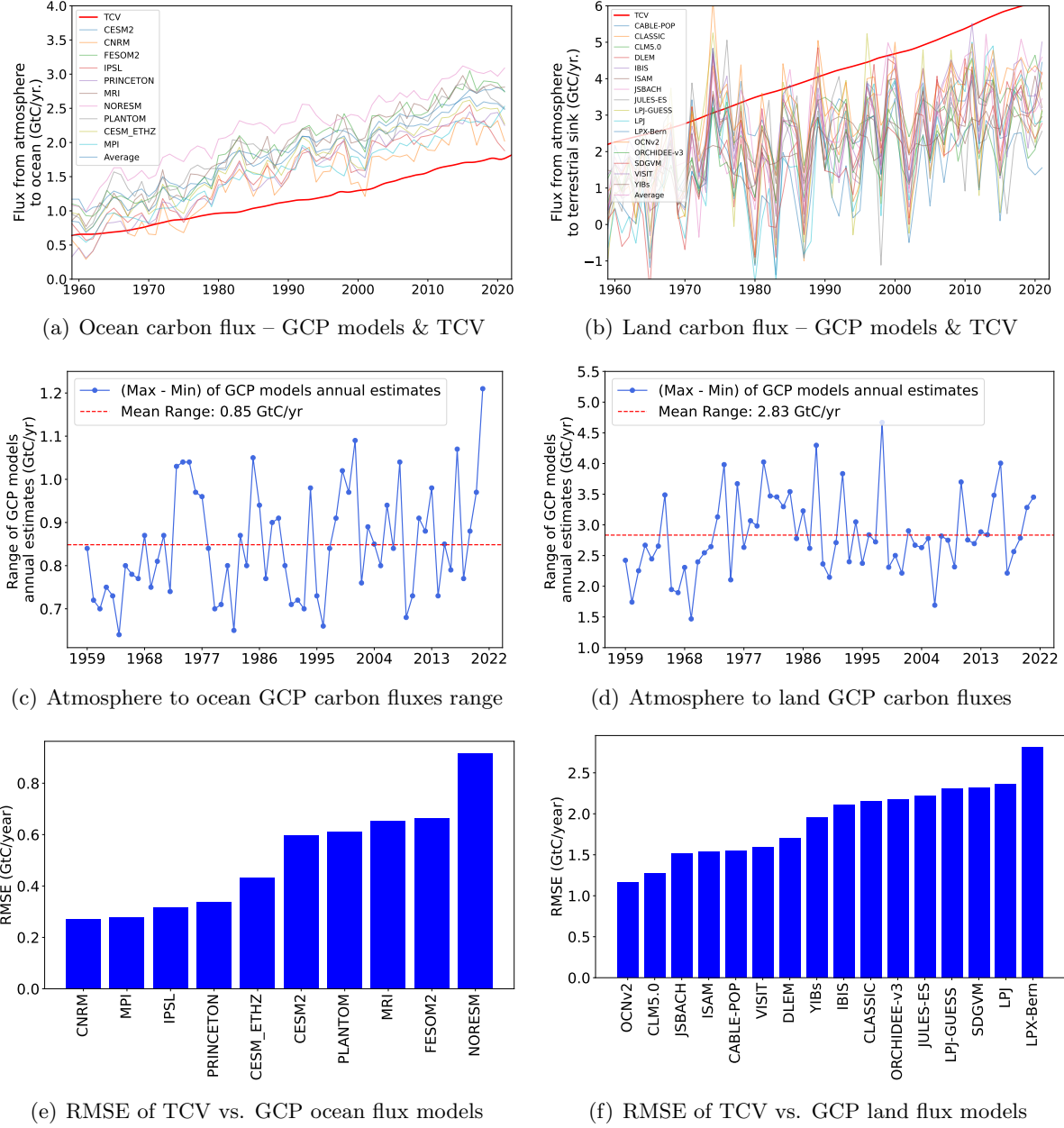


Figure S3: Variability of the GCP carbon fluxes and comparison with the TCV model fluxes. (a,b) The annually estimated carbon fluxes from all GCP models [71] (colors) for (a) atmosphere-to-ocean fluxes (eleven models), and (b) for atmosphere-to-land fluxes (16 models), over the time interval of 1959–2021, and the corresponding TCV model fluxes (solid red). (c,d) The differences each year between the maximum GCP flux vs. the corresponding minimum (solid blue) and the mean over time of the blue line (dashed red); and (e,f) the individual RMSEs between the TCV model and each GCP model.

Model Sensitivity Analysis

We study the sensitivity of the TCV model's bistability across the range of anthropogenic emissions e and the ecosystem quality degradation levels V to parameter values. With \mathbf{x} a vector of parameter values, we define the binary response as follows:

$$Y(\mathbf{x}, V) = \begin{cases} 1, & \text{if the model admits } > 1 \text{ steady states at } (\mathbf{x}, V), \\ 0, & \text{otherwise.} \end{cases} \quad (\text{S20})$$

and its trajectory-wise probability $p_{\text{bist}} = \mathbb{E}[Y]$. The one-at-a-time (OAT) sensitivity analysis plot displayed in Fig. S4 is carried out as follows for a given V value. For every parameter $\{x_i : i = 1, \dots, k\}$, we sweep x_i across a plausible interval $[x_i^{\min}, x_i^{\max}]$, while the remaining $(k-1)$ parameters are fixed at their reference values $\mathbf{x}^{(0)}$ listed in Tables S1, S2, and S3. We record the envelope of values:

$$\mathcal{R}_i = \{ Y(\mathbf{x}^{(0)} + \delta \mathbf{e}_i) \quad \text{for } \delta \in [x_i^{\min} - x_i^{(0)}, x_i^{\max} - x_i^{(0)}] \}. \quad (\text{S21})$$

Because Y is binary, $\mathcal{R}_i \subseteq \{0, 1\}$ and the extent of the colored segment on the plot is exactly $\max \mathcal{R}_{i,j} - \min \mathcal{R}_{i,j}$. A fully shaded bar across the entire parameter range signals that changing x_i can shift the model between single to bi-stable state within the emission levels tested of $-15 \leq e \leq 70$ GtC/yr. All parameter intervals $[x_i^{\min}, x_i^{\max}]$ are chosen to cover a broad set of possible values. All temperatures span a 4 K range, ocean minimum and maximum albedos span the ranges from 0.25 to 0.32, and 0.55 to 0.62, respectively, as reported in the literature [32, 33, 98], while terrestrial albedo bounds vary in a similarly broad range centered on the reference values. Incoming solar radiation varies within a ± 1.5 Wm²K⁻¹ range of the estimated preindustrial value, while oceanic and atmospheric carbon contents vary within a ± 20 GtC range with respect to reference values. All other parameters are allowed to vary within a $\pm 20\%$ range.

The output plotted in Fig. S4 provides a first filter to discriminate between parameters that never alter Y across the entire (x_i) grid vs. those that may do so. It turns out that, in fact, it is only α_{\max}^L that clearly does affect the TCV model's possessing either one or two stable steady states. For completeness, we consider the four related parameters $\mathcal{S} = \{T_{\alpha_L, \ell}, T_{\alpha_L, u}, \alpha_{\max}^L, \alpha_{\min}^L\}$ herewith.

For the reduced set of inputs \mathcal{S} , we estimate the two Sobol indices of main-effect $S_{1,i}$ and total-effect T_i [80, 81] defined by

$$S_{1,i} = \frac{\text{Var}_{x_i}[\mathbb{E}_{\mathbf{x}_{\sim i}}(Y | x_i)]}{\text{Var}(Y)}, \quad T_i = 1 - \frac{\text{Var}_{\mathbf{x}_{\sim i}}[\mathbb{E}_{x_i}(Y | \mathbf{x}_{\sim i})]}{\text{Var}(Y)}. \quad (\text{S22})$$

The main effect $S_{1,i}$ is displayed in blue bars in Fig. S5 and captures the fraction of output variance that can be removed if x_i were fixed to be a constant. The total effect T_i displayed in orange bars captures the variance share attributable to x_i when including interactions with the other parameters. Because $T_i \geq S_{1,i}$ by construction, the difference $T_i - S_{1,i}$ measures the strength of all the interaction effects that involve x_i .

Both indices are estimated here using the Saltelli [81] “AB–BA” Monte-Carlo scheme, which uses two independent $N \times k'$ base matrices A and B . For $S_{1,i}$ the unbiased Jansen estimator [82] is:

$$\hat{S}_{1,i} = \frac{\frac{1}{N} \sum_{n=1}^N f(B)_n [f(A^{(i)})_n - f(A)_n]}{\text{Var}_N(Y)}; \quad (\text{S23})$$

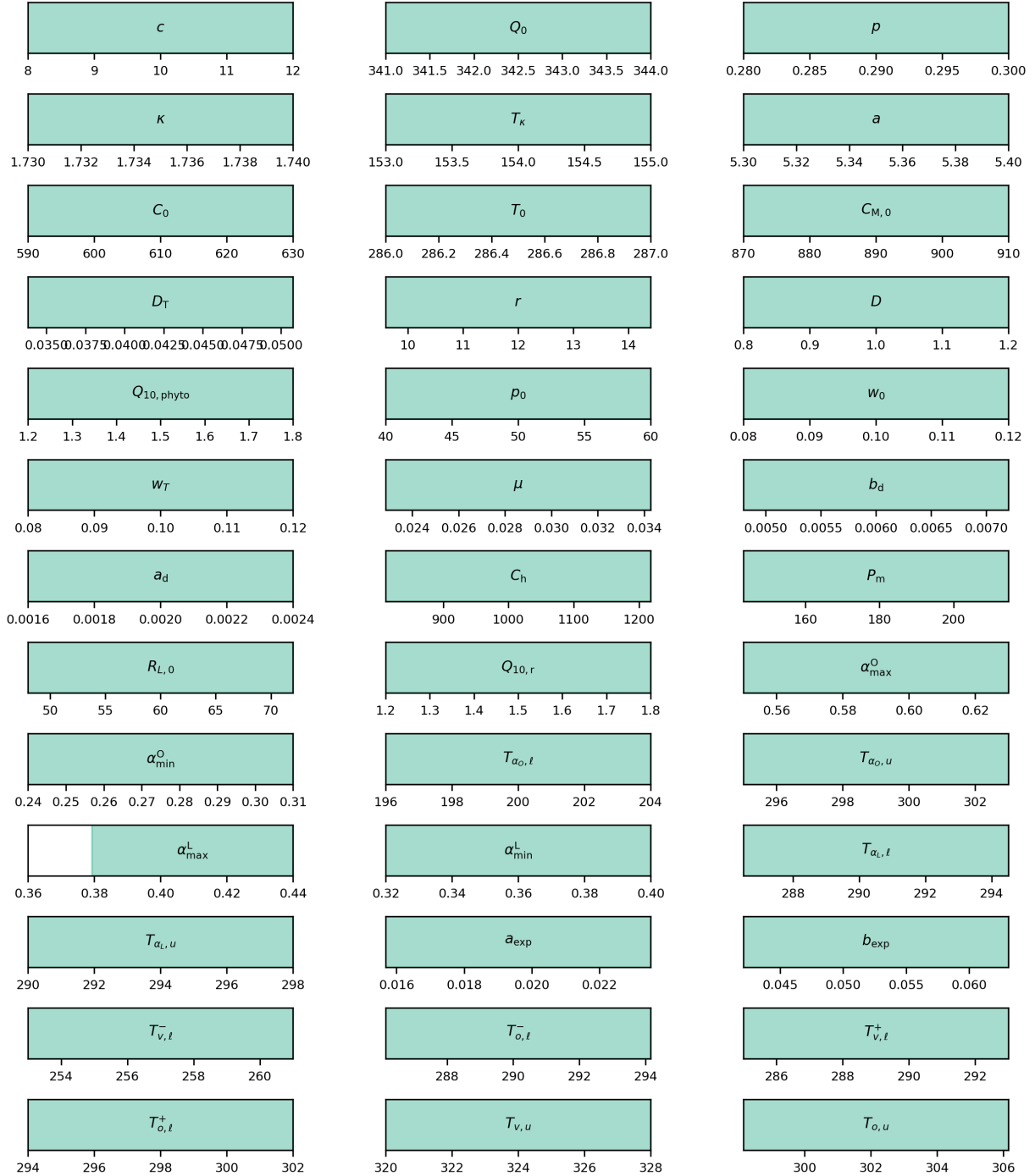


Figure S4: **Parameter ranges that yield bistability in the “one-at-a-time” (OAT) sweep.** Each subplot shows one of the 39 parameters with the x -axis spanning the range of values explored. Filled boxes indicate intervals within which the model exhibits more than one steady state, while the blank intervals correspond to a single steady state for $V = 0$.

its sampling variance, under mild regularity conditions, is

$$\text{Var}[\hat{S}_{1,i}] \simeq \frac{1}{N} \left(\mu_4 - \mu_2^2 \right), \quad (\text{S24})$$

where μ_2 and μ_4 are second- and fourth-order mixed moments that can be estimated from the same model runs [82]. Analogous expressions hold for \hat{T}_i [0]. Assuming asymptotic normality, the 95 % analytic confidence intervals are computed as follows:

$$\hat{S} \pm 1.96 \sqrt{\text{Var}[\hat{S}]}, \quad \hat{T} \pm 1.96 \sqrt{\text{Var}[\hat{T}]} \quad (\text{S25})$$

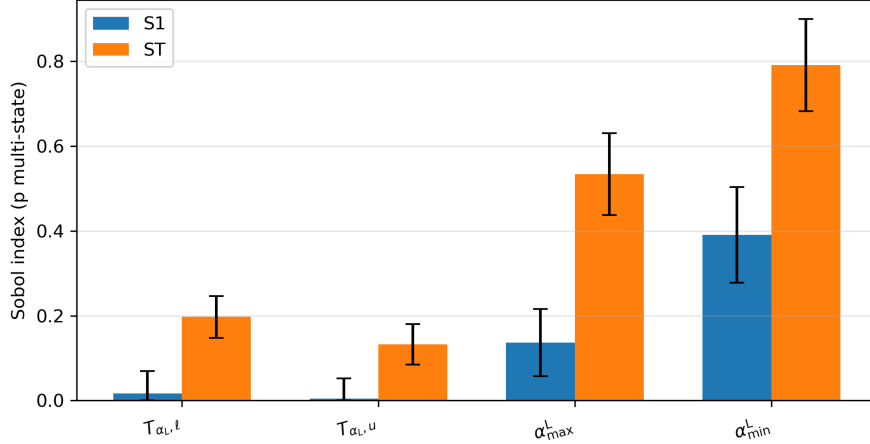


Figure S5: **Variance-based Sobol sensitivity analysis of the TCV model to selected parameters.** First-order (S_1 , blue bar) and total-effect (S_T , orange bar) Sobol sensitivity indices of the probability of bistable behaviour (p_{bist}) at $V = 0$. Bars show point estimates, and error bars denote analytic 95% confidence intervals. The parameter α_L^{max} dominates both individually (S_1) and including higher-order interactions (S_T), whereas the remaining parameters contribute only weakly to the variance of p_{bist} .

The narrow intervals on the three parameters $\mathcal{S} \setminus \{\alpha_L^{min}\}$ confirm that α_L^{min} alone dominates the output variance, while the other factors contribute only marginally. These results are entirely consistent with the qualitative OAT screening stage illustrated in Fig. S4. In order to identify which parameters interact dominate the total variance, for any two inputs x_i, x_j ($i < j$) of subset \mathcal{S} we also report the second-order Sobol index defined as follows:

$$S_{2,ij} = \frac{\text{Var}_{x_i, x_j} [\mathbb{E}_{\mathbf{x} \sim \{i, j\}} (Y | x_i, x_j)] - V_i - V_j}{\text{Var}(Y)}, \quad (\text{S26})$$

where $V_i = \text{Var}_{x_i} [\mathbb{E}(Y | x_i)]$. $S_{2,ij}$ measures the fraction of variance that can only be explained by the joint variation of x_i and x_j and cannot be attributed to either parameter alone. Using the extended Saltelli ‘‘AB–BA’’ sampling scheme, the unbiased estimator [0] is defined by:

$$\hat{S}_{2,ij} = \frac{\frac{1}{N} \sum_{n=1}^N [f(B^{(i)})_n - f(A)_n] [f(A^{(j)})_n - f(A)_n]}{\widehat{\text{Var}}_N(Y)}. \quad (\text{S27})$$

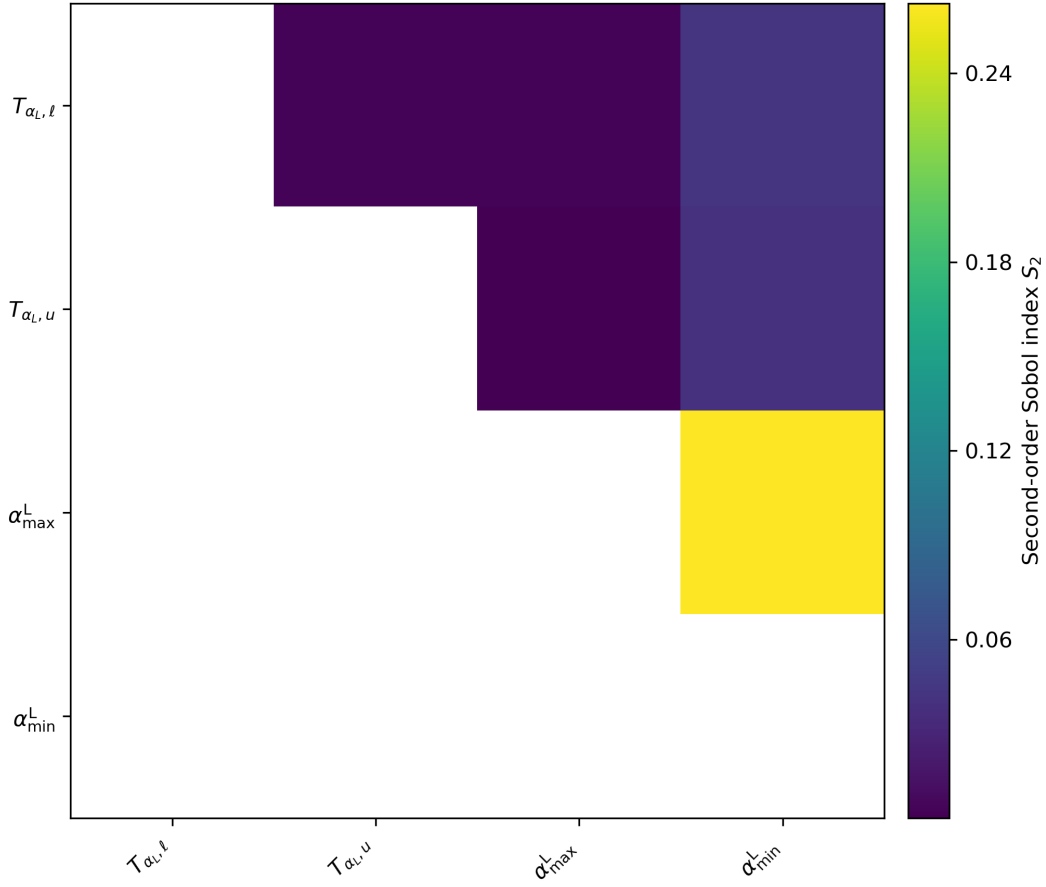


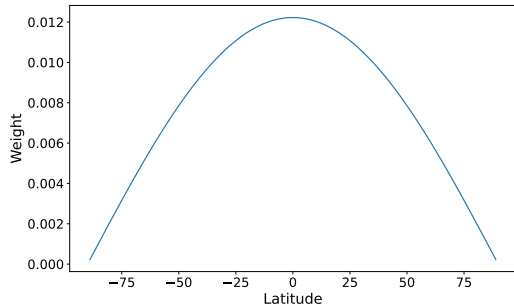
Figure S6: **Pairwise TCV terrestrial albedo parameters interaction Sobol indices (S_2).** Second-order Sobol indices of pairwise interactions for the four parameters set \mathcal{S} . Colour scale indicates the proportion of ST output variance that can be attributed only to the interaction of each parameter pair. The interaction $\alpha_{\min}^L \times \alpha_{\max}^L$ of terrestrial albedo bounds dominate and accounts for $\approx 25\%$ of the variance, while interactions involving the threshold temperatures ($T_{\alpha_L, \ell}$, $T_{\alpha_L, u}$) account for less than $\approx 5\%$.

Figure S6 shows that the only significant pairwise interaction is $\alpha_{\min}^L \times \alpha_{\max}^L$ between the two terrestrial albedo bounds with $S_{2, \alpha_{\min}^L \times \alpha_{\max}^L} \approx 0.25$ indicating that approximately 25 % of the output (bistability) variance arises from the non-additive effect of modifying the two terrestrial albedo bounds jointly. All other pairwise parameter second order Sobol indices have $|S_{2,ij}| < 0.05$ indicating negligible interaction. Combined with the large S_1 and ST gap for α_{\min}^L (Fig. S5), this result confirms that the bistability of the TCV model is primarily sensitive to the contrast of terrestrial albedo bounds rather than by the threshold temperatures $T_{\alpha_L, \ell}$ and $T_{\alpha_L, u}$.

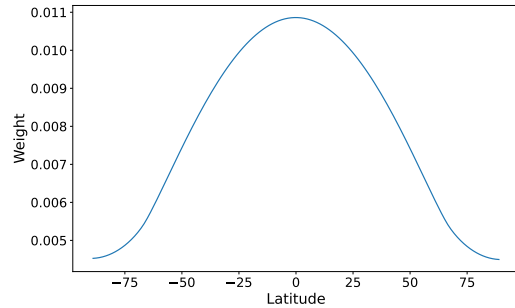
Global average land albedo latitudinal weights

Visualization of the tipping to the hothouse

The following three videos are attached to the present submission. The first two videos are made using the DAE model governed by the two ODEs (2a) and (2b), with V fixed. In the third video, $V = V(t)$ is allowed to change according to the ODE (2c) of the DAE model. In all three cases, the emissions $e = e(t)$ evolve according to the RCP 8.5 scenario that corresponds to Fig. 6(c).



(a) Latitudinal weights for area averaging



(b) Latitudinal weights accounting to account for annual change of cumulative radiation ($\text{Wm}^{-2}\text{yr}^{-1}$), as a function of latitude

Figure S7: **Global average terrestrial surface albedo computation latitudinal weights.** The global averaged albedo is computed by carrying out a weighted sum of grid-level surface albedo, considering both (a) area weighting; and (b) annual cumulative radiation as a function of latitude [116].

In all three videos, the left panel shows the changes in the model’s nullclines $F_1(T, C) = 0$ and $F_2(T, C) = 0$, along with the trajectory of the actual solution $(T(t), C(t))$ in the corresponding model’s phase plane (T, C) . The right panel illustrates the evolution of the solution’s temperature $T(t)$ in time. The initial point of the trajectory being computed is taken close to, but not identical to the climate for preindustrial conditions in 1750 and computations are carried out till 2200. Note that, at the end of the simulation, $e(t) = 28.8 \text{ GtC/yr}$ and the corresponding temperature of P_2 is roughly 14 K higher than at $e = 0$. A rapid shift of 10 K from the present-climate-like steady state to a hothouse Earth steady state starts approximately in 2085 and it is completed over a 20-year time interval.

The short video labeled `TCV_video-V=V(t)` displays the results of a simulation that is carried out with the complete DAE model governed by equations (2), i.e., the ecosystem degradation $V = V(t)$ varies in time following equation (2c) as $e(t)$ follows the anthropogenic RCP 8.5 emission scenario. The video documents the merger of the stable and unstable fixed points P_1 and P_3 that leads to the sudden tipping to the hothouse Earth, as well as the overshoot of the globally averaged temperature $T(t)$ before reaching its new equilibrium at roughly 12 K above the preindustrial level. Notice the good fit to the observed global temperatures (black line) over the instrumental interval 1880–2022.

Author contributions

E.C., M.G., and J.R. designed the study, E.C. and J.R. carried out the computations, and all three authors participated in the analysis of the results and in the writing.

Competing interests

The authors declare no competing interests.